POLITECNICO
MILANO 1863

SCUOLA DI INGEGNERIA INDUSTRIALE
E DELL'INFORMAZIONE

Analytical modelling of Conjugate Heat Transfer for the nasal flow

Tesi di Laurea Magistrale in
Aeronautical Engineering - Ingegneria Aeronautica

Author: **Maria Vittoria Pennisi**

Student ID: 991651
Advisor: Prof. Maurizio Quadrio
Co-advisor: Prof. Jan Pralits
Academic Year: 2022-2023

Abstract

Conjugate Heat Transfer (CHT) has primarily importance in scenarios involving connected sub-domains governed by different heat transfer equations, such as human respiration, where heat exchange occurs between inspired air (fluid) and respiratory mucous (considered as a solid in this work). The choice of a CHT approach is mandatory when a higher level of accuracy is required and a constant wall temperature condition fails to provide a reliable solution. However, CHT entails higher computational costs, due to additional equations and sub-domains coupling, and longer pre-processing time. To address these challenges, this study employs asymptotic homogenization theory, applicable given the presence of well separated length scales, to derive an effective temperature boundary condition for smooth solid-fluid interfaces, eliminating the need for resolving the thin solid layer.

Firstly, validation simulations have been conducted with simple channel geometries and have exhibit strong agreement between the results obtained using the homogenized boundary condition and those from full CHT simulations, particularly for thinner solid layers. Subsequently, the derived boundary condition is applied to nasal airflow simulations, effectively replacing the need to fully resolve the thin mucous layer. Several simulations have been performed by varying the environmental temperature, to evaluate the correlation of the error, defined as the difference between the temperature calculated with the homogenized boundary condition and with full CHT simulations, with the increase in temperature difference between the exterior and the human body. It has been found that the error increases as the thermal jump in the domain increases. However, the relative percentage error, with respect to the temperature jump, remains constant, reaching a maximum of 1% only in some sections of the nose that are particularly thin and highly curved. Using the derived model, problems involving conjugate heat transfer can be solved with approximately 30% reduced computational time and 40% reduced cost, while ensuring greater accuracy compared to when a constant wall temperature boundary condition is employed.

Keywords: nasal flow, CFD, homogenization, CHT, boundary condition

Abstract in lingua italiana

Lo scambio termico coniugato (CHT) riveste un'importanza cruciale in scenari che coinvolgono sotto domini interconnessi e il trasferimento di calore, come ad esempio nella respirazione umana, dove si verifica lo scambio termico tra l'aria inspirata (fluido) e la mucosa respiratoria (considerata solida in questo lavoro). L'adozione di un approccio CHT è necessaria quando si richiede un livello di precisione elevato e imporre semplicemente una condizione di temperatura costante a parete non fornisce una soluzione realistica. Tuttavia, il CHT comporta un maggiore costo e tempo computazionale, inoltre richiede una realizzazione del dominio di calcolo più complicata. Per questi motivi, questo studio utilizza la teoria dell'omogeneizzazione asintotica per derivare una condizione al contorno di temperatura da imporre all'interfaccia tra solido e fluido per una parete liscia, eliminando la necessità di simulare il sottile strato di solido.
A scopo di validazione, sono eseguite delle simulazioni con geometrie semplificate di condotti. I risultati, ottenuti utilizzando la condizione al contorno omogeneizzata e le simulazioni CHT complete, hanno mostrato un ottimo accordo, soprattutto per uno spessore di solido sottile. Successivamente, la condizione al contorno è stata applicata al caso del naso. Sono state condotte diverse simulazioni variando la temperatura ambiente, per valutare la correlazione dell'errore, definito come la differenza tra la temperatura calcolata con la condizione al contorno omogeneizzata e con le simulazioni CHT complete, con l'incremento della differenza di temperatura tra l'esterno e il corpo umano. L'errore aumenta all'aumentare del salto termico nel dominio; tuttavia, l'errore percentuale relativo al salto termico rimane costante, raggiungendo un massimo dell'1% in sezioni particolarmente sottili e fortemente curve della cavità nasale. Utilizzando il modello derivato in questa tesi, i problemi di scambio termico coniugato possono essere risolti con circa il 30% di riduzione del tempo di calcolo e il 40% di riduzione del costo computazionale, garantendo una maggiore accuratezza rispetto a una condizione di temperatura costante.

Parole chiave: flusso nella cavità nasale, CFD, omogeneizzazione, CHT, condizione al contorno

Contents

Abstract **i**

Abstract in lingua italiana **ii**

Contents **iii**

1 Introduction **1**

2 Homogenization **4**
2.1 Governing equations 4
2.2 The homogenization-based upscaling 6
2.2.1 Limiting case of smooth surface 9

3 Simulations set-up **14**
3.1 Model 14
3.1.1 Simple channels 14
3.1.2 Human nose 15
3.2 Grid generation 16
3.3 Solver settings 18
3.4 Boundary conditions 20

4 Results **22**
4.1 Simple channels 22
4.2 Human nose 24

5 Conclusions **32**

Bibliography **34**

A Appendix A **37**

List of Figures **43**

List of Tables **45**

Listings **46**

Acknowledgements **47**

1 | Introduction

Computational Fluid Dynamics (CFD) is becoming increasingly common as a support for investigating bio-mechanical problems, including the study of nasal airways. This tool allows for a detailed analysis of the flow characteristics in the respiratory system of each specific patient, as the models used are reconstructed from images acquired through Computed Tomography (CT) scan. Based on the information obtained from fluid dynamics simulations, the surgeon has the opportunity to identify the most critical areas where intervention is necessary and perform procedures with a higher success rate, which is not guaranteed in this field, especially in the long term [11]. In this context, the OpenNOSE project, which is a collaboration involving Politecnico di Milano, University of Genova, University of Milan and the otolaryngology group at San Paolo Hospital, is developed. This project aims to create a reliable diagnostic procedure for issues related to nasal airways employing fluid dynamics simulations.

A relevant aspect of the nasal flow is represented by the phenomenon of heat exchange that happens in the upper airways. Within the framework of the OpenNOSE project, two thesis works have specifically focused on the heat exchange occurring in the nose. In [23], the effects of temperature are evaluated assuming that the airways walls are all at a constant temperature, equal to that of the human body; indeed, a constant wall temperature boundary condition is widely applied in the literature concerning this topic [12, 15, 17, 20]. However, this assumption may be a significant simplification since the thermoregulation function of the nose is a rather complex mechanism. For this reason, in [16], this simplifying hypothesis is questioned, proposing a more realistic model to simulate heat exchange in the nasal cavity by solving a complete conjugate heat transfer problem between the mucous layer lining the nasal walls (Figure 1.1) and the airflow. This analysis resulted in a temperature distribution on the nasal cavity walls that can be considered more accurate than the assumption of uniform temperature. It is important to highlight that the ability to identify the coldest areas of the nasal cavity surface tissue is clinically significant, since a colder mucous implies more fragile and inclined to bleeding capillaries, and this is not possible when a constant wall temperature boundary condition is employed.

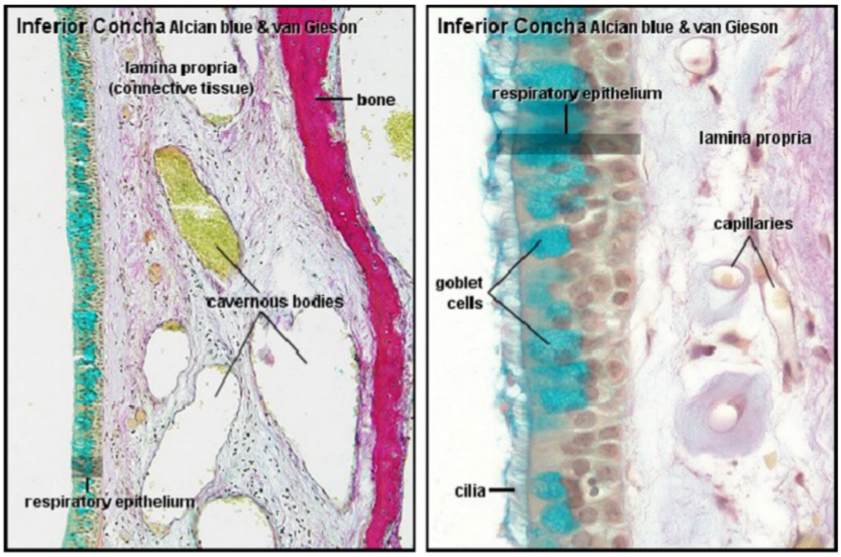

Figure 1.1: Respiratory mucous histology inside the human nose. The upper airways are characterized by a thin layer (respiratory mucous) immersed in an airflow, where heat transfer is involved.

Conjugate Heat Transfer (CHT) provides higher accuracy compared to a constant temperature boundary condition, but has some downsides: the computational cost and time are higher, since additional equations should be solved and a coupling between the subdomains must be performed for each iteration, moreover the pre-processing of the domain takes longer time because there is an additional sub-domain to take care of. Its drawbacks are emphasised in the case of the nose, because the solid mucous layer is thin and requires many cells to be well resolved; in addition, the complexity of the nasal cavity geometry (Figure 1.2) causes issues when it comes to adding the solid layer, seeing that self-intersections may occur degrading the geometry quality and the meshing process difficulty drastically increases. This makes working with real geometries, acquired through CT scan, difficult and the only possible approach is to reduce the number of details making a less reliable, but feasible, simulation.
The goal of the present thesis is to model the coupled CHT problem, between the mucous layer and the airflow inside the nasal cavity, with an equivalent, analytical, boundary condition derived with asymptotic homogenization theory. In this framework, homogenization plays an important role, indeed the use of equivalent boundary conditions allows to have a good solution, aligned to the one obtained with conjugate heat transfer, without fully resolving the solid layer [5]. This guarantees a reduced computational cost, given that it avoids solving the complete set of coupled differential equations, and eliminates the need of smoothing and simplifying the original geometry, that is necessary to include the solid mucous layer in the model.

The asymptotic multiscale homogenization approach is a theoretical method used to simplify the study of surfaces with rapidly changing properties, like roughness and porosity, so in the presence of well separated length scales [7, 10]. The method relies on using asymptotic expansions of the problem variables based on a carefully chosen small parameter. This parameter is linked to the existence of distinctly separated length scales, such as a microscopic length scale (ℓ) and a macroscopic length scale ($H >> \ell$). By defining the parameter $\epsilon = \ell/H << 1$, solutions to the problem can be found with varying degrees of accuracy based on different orders of ϵ. By using this approach, it is possible to avoid precisely modelling the motion around small solid protrusions or the thin mucous layer in the human nose case.

In this contribution, it is firstly carried out an analytical derivation through homogenization of the equivalent boundary condition for a smooth interface between solid and fluid, then the obtained boundary condition is tested with simplified geometries, in order to validate it through a comparison with results acquired via CHT simulations and to understand the limitations of this formulation. Subsequently, the boundary condition is applied to the case of the nose. The results obtained with this model are compared with those obtained with complete CHT simulations to assess its reliability for different ambient temperatures. In all simulations, only the inspiration phase is considered, because the effects of nasal conditioning are more noticeable. Therefore, in the context of the OpenNOSE project, this study aims to take a further step in the search for an upper airway model that is both realistic and efficient, reducing the computational effort.

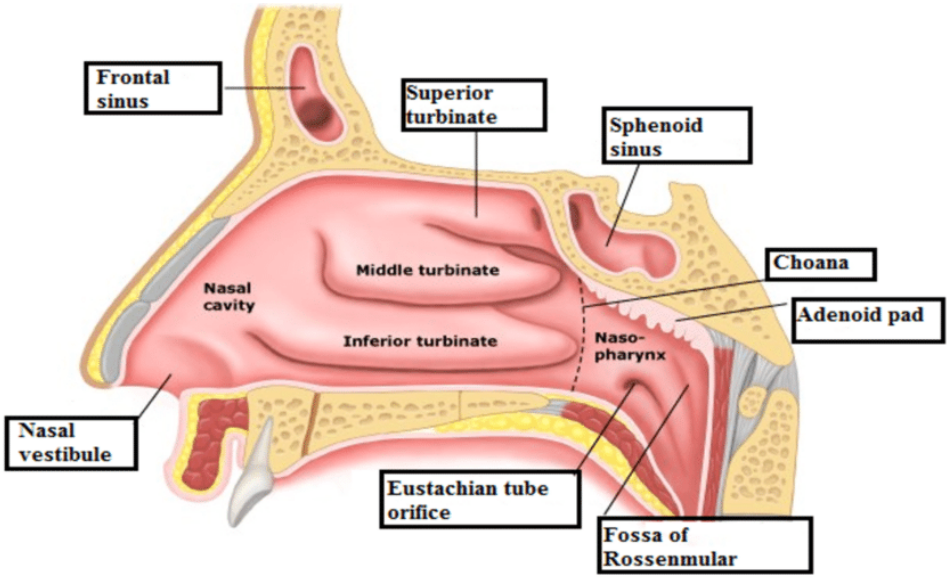

Figure 1.2: Nasal cavity anatomy.

2 | Homogenization

The asymptotic multiscale homogenization approach is a theoretical framework through which the rapidly varying properties of a surface (related to, for instance, roughness) can be replaced by upscaled properties (such as slip length), which contribute to the definition of effective boundary conditions at a fictitious plane interface next to the physical textured boundaries. The macroscale behaviour of the flow is then targeted, bypassing the need to fully resolve the motion between or in close vicinity of the solid protrusions. This technique has been known and used by mathematicians for a long time; however, in more recent years, it has been rediscovered and applied to a variety of physically relevant cases.

The present study focuses on employing asymptotic homogenization to analyse the airflow inside the nasal cavity, where heat exchange occurs between the respiratory mucous (considered as a smooth and thin solid layer) and the inspired air. In order to achieve this, it is firstly necessary to derive the homogenized boundary condition in the case of a smooth solid boundary delimiting a straight channel. The methodology adopted is inspired by researches conducted by Ahmed, Bottaro and Tanda [4, 5] and Ahmed [2], which are focused on deriving and validating effective velocity and temperature boundary conditions, but for rib-roughened surfaces.

In this chapter, the physical problem is described, the governing equations are given and the formal expression of the effective boundary condition is derived in the limiting case of a smooth solid boundary. It is also added a brief explanation of the fully-rough case, since it is the starting point of the methodology employed in this work. The homogenized boundary condition for the smooth limit will be implemented in *OpenFOAM* and tested by comparing it with complete CHT simulations, for simple channel geometries and in the case of the nose.

2.1. Governing equations

The hydrodynamic and thermal interaction between a fluid flowing in a channel (externally forced in $\hat{x}$) and the delimiting solid boundary is considered, as illustrated in Figure

2.1. The conjugate heat transfer problem, including thermal conduction in the solid region and heat transfer by convection to the fluid phase is analysed. The dimensional mass, momentum and energy conservation equations governing the steady, incompressible, Newtonian flow at any point $(\hat{x}_1, \hat{x}_2, \hat{x}_3) = (\hat{x}, \hat{y}, \hat{z})$ in the fluid domain (β) are, respectively:

$$\frac{\partial \hat{u}_i}{\partial \hat{x}_i} = 0, \tag{2.1}$$

$$\rho\, \hat{u}_j \frac{\partial \hat{u}_i}{\partial \hat{x}_j} = -\frac{\partial \hat{P}}{\partial \hat{x}_i} + \mu\, \frac{\partial^2 \hat{u}_i}{\partial \hat{x}_j^2}, \tag{2.2}$$

$$\hat{u}_j \frac{\partial \hat{T}}{\partial \hat{x}_j} = \left(\frac{k_f}{\rho c_p}\right) \frac{\partial^2 \hat{T}}{\partial \hat{x}_j^2}, \tag{2.3}$$

with $\hat{\mathbf{u}} = (\hat{u}_1, \hat{u}_2, \hat{u}_3)$ the velocity vector, $\hat{P}$ the pressure and $\hat{T}$ the temperature. The fluid properties, i.e. the density ρ, the dynamic viscosity μ, the thermal conductivity k_f, and the specific heat c_p, are assumed constant, neglecting variations in their values with temperature along and across the channel. Moving to the solid bounding layers (σ), the steady thermal conduction is governed by the following Laplace's equation describing spatial variations of the temperature $\hat{\mathcal{T}}$:

$$\frac{\partial^2 \hat{\mathcal{T}}}{\partial \hat{x}_j^2} = 0. \tag{2.4}$$

A uniform, prescribed temperature $\hat{\mathcal{T}}_C$ is imposed at the outer surfaces $(\mathcal{I}_C)$ of the bounding plates, i.e., at $\hat{y} = -e$ (for lower layer) and $\hat{y} = h + H + h' + e'$ (for upper layer), while the side surfaces of the plates ($\mathcal{I}_{ad}$, located at the channel inlet/outlet) are assumed adiabatic. Continuity of temperature and heat flux is defined along the solid-fluid interfaces $(\mathcal{I}_{\sigma\beta})$. The aforementioned boundary conditions can be expressed as follows:

$$\begin{cases} \hat{\mathcal{T}} = \hat{\mathcal{T}}_C & \text{at } \mathcal{I}_C, \\ \dfrac{\partial \hat{\mathcal{T}}}{\partial \hat{x}_1} = 0 & \text{at } \mathcal{I}_{ad}, \\ \hat{T} = \hat{\mathcal{T}}, \;\; \dfrac{\partial \hat{T}}{\partial \hat{n}} = \kappa \dfrac{\partial \hat{\mathcal{T}}}{\partial \hat{n}} & \text{at } \mathcal{I}_{\sigma\beta}, \end{cases} \tag{2.5}$$

with $\kappa = k_s/k_f$ the solid-to-fluid thermal conductivity ratio and $\hat{n}$ the dimensional dis-

tance in the direction normal to $\mathcal{I}_{\sigma\beta}$ at any point. In addition, the fluid is assumed to enter the channel at a uniform velocity $\hat{u}_1\big|_{\hat{x}_1=0} = \hat{u}_{inlet}$ and temperature $\hat{T}\big|_{\hat{x}_1=0} = \hat{T}_{inlet}$, and a no-slip velocity boundary condition is enforced at $\mathcal{I}_{\sigma\beta}$, while the static pressure is set to zero at the outlet. The fields are periodic in the spanwise direction, $\hat{x}_3 = \hat{z}$.

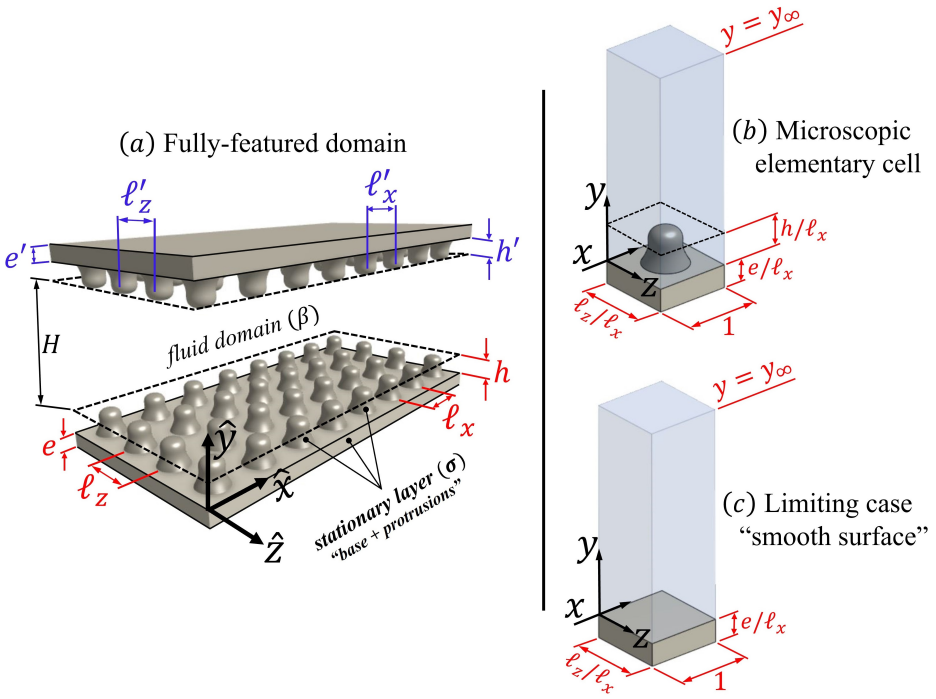

Figure 2.1: Sketch of the problem under consideration. The plane interfaces delimited by dashed lines constitute the *virtual boundaries* where effective conditions are to be enforced.

2.2. The homogenization-based upscaling

The analysis described above is capable of resolving the fully-featured fields in the fluid and the solid domains; however, when the macroscale behaviour of the channel flow is of particular interest, it is advantageous from a computational point of view to implement an upscaling approach that mimics the presence of a rough walls or of a thin and smooth solid layer, via application of effective velocity and temperature boundary conditions at fictitious plane interfaces next to the physical boundaries. In this section, before explaining their derivation in the limit case of a smooth solid boundary, the multiscale homogenization approach derived and validated in [4–6] for rib-roughened surfaces is presented. It is shown here slightly modified to neglect buoyancy effects, since forced instead of natural convection is considered in this study to enable analysis in the case of

the nasal flow. In the homogenization-based simulations, the macroscopic variables ($\ddot{u}_i$, $\ddot{P}$, $\ddot{T}$) are targeted in the fluid domain bounded by the virtual interfaces; these fields correspond, if accurately evaluated, to the running averages ($< \hat{u}_i >$, $< \hat{P} >$, $< \hat{T} >$) of the variables resolved in the fully-featured simulations ($\hat{u}_i$, $\hat{P}$, $\hat{T}$). Taking the case of a wall roughened with protrusions of pitch distances ℓ_x and ℓ_z (refer to Figure 2.1(a)) as a representative example, one can define the running-average temperature at a point $\Psi : (\hat{x}_\psi, \hat{y}_\psi, \hat{z}_\psi)$, located in the fluid domain beyond the roughness layer, by averaging the fully-resolved field over a rectangular $\hat{x} - \hat{z}$ region of dimensions $\ell_x \times \ell_z$, whose center is the point Ψ, as follows:

$$< T > \big|_{\hat{x}_\psi, \hat{y}_\psi, \hat{z}_\psi} = \frac{1}{\ell_x \times \ell_z} \int_{\hat{x}_\psi - \ell_x/2}^{\hat{x}_\psi + \ell_z/2} \int_{\hat{z}_\psi - \ell_z/2}^{\hat{z}_\psi + \ell_z/2} \hat{T}(\hat{x}, \hat{y}_\psi, \hat{z})\, d\hat{z}\, d\hat{x} \approx \ddot{T}\big|_{\hat{x}_\psi, \hat{y}_\psi, \hat{z}_\psi}, \tag{2.6}$$

and likewise for the velocity and pressure.

While the typical interaction between the forced flow and the roughness elements is generally three-dimensional, and the fully-resolved velocity field is three-directional (taking into account spanwise deflection of the streamlines around the protrusions), the problem can be considered two-dimensional from the macroscopic point of view, including development of the viscous and thermal boundary layers along the streamwise direction, $\hat{x}_1$, and variations of the fields in the wall-normal direction, $\hat{x}_2$. Moreover, the macroscopic (averaged) spanwise velocity component, $\ddot{u}_3$, is expected to vanish, provided that the microscopic pattern of the textured boundaries has no preferential orientation relative to the direction of the external forcing, as in the case sketched in Figure 2.1. The reader is strongly encouraged to refer to [3, 22] for further discussions/elaboration. Thanks to the above-mentioned simplifications, it is sufficient to run the homogenization-based simulation over a two-dimensional ($\hat{x}_1 - \hat{x}_2$) plane through which the fields $\ddot{u}_1$, $\ddot{u}_2$, and $\ddot{T}$ are to be evaluated. The spatial variations of these variables are governed by:

$$\frac{\partial \ddot{u}_i}{\partial \hat{x}_i} = 0, \tag{2.7}$$

$$\rho\, \ddot{u}_j \frac{\partial \ddot{u}_i}{\partial \hat{x}_j} = -\frac{\partial \ddot{P}}{\partial \hat{x}_i} + \mu\, \frac{\partial^2 \ddot{u}_i}{\partial \hat{x}_j^2}, \tag{2.8}$$

$$\ddot{u}_j \frac{\partial \ddot{T}}{\partial \hat{x}_j} = \left(\frac{k_f}{\rho c_p}\right) \frac{\partial^2 \ddot{T}}{\partial \hat{x}_j^2}, \tag{2.9}$$

subject to *effective* boundary conditions of $\ddot{u}_1$, $\ddot{u}_2$, and $\ddot{T}$ along the virtual interfaces, chosen here at $\hat{y} = h$ and $\hat{y} = h + H$, i.e. the planes passing by the tips/crests of the protrusions. These upscaled conditions are already available in the literature (with simple adjustment) via application of asymptotic homogenization [5, 6], and their validity is contingent on the presence of well-separated length scales (for instance, the pitch distance of the roughness pattern, ℓ, as a microscopic length scale and the channel height, H, as a macroscopic length scale), such that a small parameter, $\epsilon = \ell/H << 1$, can be defined. Under steady flow conditions, the transpiration velocity at the fictitious interfaces is neglected by setting $\ddot{u}_2\big|_{\hat{x}_2=h}$ and $\ddot{u}_2\big|_{\hat{x}_2=h+H}$ to zero, while the following boundary conditions of $\ddot{u}_1$ and $\ddot{T}$, second-order accurate in terms of ϵ, are imposed:

$$\ddot{u}_1\bigg|_{\hat{x}_2=h} \approx \Lambda_x \left.\frac{\partial \ddot{u}_1}{\partial \hat{x}_2}\right|_{\hat{x}_2=h} + \frac{M_{12}}{\mu}\frac{\partial}{\partial \hat{x}_1}\left(-\ddot{P} + 2\mu\frac{\partial \ddot{u}_2}{\partial \hat{x}_2}\right)\bigg|_{\hat{x}_2=h}, \tag{2.10}$$

$$\ddot{T}\bigg|_{\hat{x}_2=h} \approx \hat{\mathcal{T}}_C + \Lambda_\theta \left.\frac{\partial \ddot{T}}{\partial \hat{x}_2}\right|_{\hat{x}_2=h}, \tag{2.11}$$

and likewise for the top interface. The model parameters Λ_x, Λ_θ, and M_{12} are the dimensional Navier-slip, thermal-slip, and interface permeability coefficients, respectively. These upscaled coefficients correspond to the product of their dimensionless counterparts (λ_x, λ_θ, and m_{12}) times either a length (for the slip parameters) or a surface area (for the interface permeability) as follows:

$$\Lambda_x = \lambda_x\,\ell_x, \quad \Lambda_\theta = \lambda_\theta\,\ell_x, \quad M_{12} = m_{12}\,\ell_x^2, \tag{2.12}$$

It is important to highlight that the homogenization-based model is free of any empirical parameters, since the dimensionless macroscopic coefficients of interest can be evaluated by solving *ad hoc* auxiliary problems governing the distribution of closure variables over an elementary cell, representative of the microscopic domain, with the dimensions normalized by the microscopic length scale as sketched in Figure 2.1(b). The dimensionless microscopic coordinates $x_i = \hat{x}_i/\ell_x$ are thus defined at the bottom wall, and likewise for the top surface. In particular, it is sufficient at each boundary to solve a Stokes-like and a Laplace-like systems governing the auxiliary variables ($u_i^\dagger$, $p^\dagger$) and ($\theta^\dagger$, $\phi^\dagger$), respectively, in order to evaluate λ_x and m_{12} (based on $u_1^\dagger$) and λ_θ (based on $\theta^\dagger$). Such closure problems read:

$$\begin{cases} \partial_i u_i^\dagger = 0 \qquad \text{in fluid domain } (\beta), \\ -\partial_i p^\dagger + \partial_j^2 u_i^\dagger = 0 \qquad \text{in fluid domain } (\beta), \\ -p^\dagger \delta_{i2} + \partial_2 u_i^\dagger + \partial_i u_2^\dagger = \delta_{i1} \qquad \text{at } \ y = y_\infty, \\ u_i^\dagger = 0 \qquad \text{at } \ \mathcal{I}_{\sigma\beta}, \end{cases} \tag{2.13}$$

and

$$\begin{cases} \partial_i^2 \theta^\dagger = 0 \qquad \text{in fluid domain } (\beta), \\ \partial_i^2 \phi^\dagger = 0 \qquad \text{in solid domain } (\sigma), \\ \partial_2 \theta^\dagger = 1 \qquad \text{at } \ y = y_\infty, \\ \theta^\dagger = \phi^\dagger, \ \ \frac{\partial \theta^\dagger}{\partial n} = \kappa \frac{\partial \phi^\dagger}{\partial n} \qquad \text{at } \ \mathcal{I}_{\sigma\beta}, \\ \phi^\dagger = 0 \qquad \text{at } \ \mathcal{I}_C, \end{cases} \tag{2.14}$$

plus periodicity of all the dependent variables in the x and z directions. The operators used above are defined as $\partial_i = \dfrac{\partial}{\partial x_i}$ and $\partial_i^2 = \dfrac{\partial^2}{\partial x_i^2}$. The basic derivation requires that the closure problems are to be solved in a microscopic unit cell with the matching interface, at $y = y_\infty$, set sufficiently far from the wall (for instance, $y_\infty \approx 5$). The upscaled coefficients for a matching interface of choice at $y_\infty = h/\ell_x$ (i.e., the plane of crests) can be estimated directly from the following averaging operations:

$$\lambda_x = \frac{1}{\mathcal{A}_{xz}} \int_{\mathcal{S}_0} u_1^\dagger \, dA, \quad m_{12} = \frac{1}{\mathcal{A}_{xz}} \int_{\mathcal{V}_0} u_1^\dagger \, dV, \tag{2.15}$$

$$\lambda_\theta = \frac{1}{\mathcal{A}_{xz}} \int_{\mathcal{S}_0} \theta^\dagger \, dA, \tag{2.16}$$

where $\mathcal{S}_0$ and $\mathcal{V}_0$ are, respectively, the virtual surface at and the fluid volume below the plane $y = h/\ell_x$, and $\mathcal{A}_{xz}$ is the normalized area of an $x - z$ cross section of the unit cell ($\mathcal{A}_{xz} = 1 \times \dfrac{\ell_z}{\ell_x}$). Clearly, the systems (2.13) and (2.14), together with the relations (2.15) and (2.16), render the coefficients λ_x and m_{12} dependent merely on the geometric details of the wall texture, whereas the thermal-slip coefficient λ_θ depends, in addition, on the solid-to-fluid thermal conductivity ratio, κ. Values of these parameters are available in [2, 4–6] for rough boundaries of different geometric/thermal characteristics.

2.2.1. Limiting case of smooth surface

For the limiting case of a surface without roughness, it is possible to derive an analytical expression for the homogenized solution. In this paragraph, its derivation is extensively covered, starting from the procedure described in Section 2.2 and specializing it for the

case of a plain solid boundary.
Given that the solid layer and the channel are characterized by well-separated length scales, i.e. $e << H$ (Figure 2.1), upscaling of the problem is sought by decomposing the flow domain into two subregions (microscopic/macroscopic). The microscopic domain includes the solid layer and the part of the fluid domain immediately above it. For this geometry, i.e. the smooth wall, the virtual boundary coincides with the solid-fluid interface where there is a condition of non-penetration and no-slip, hence there the velocity is set to zero. For this reason, unlike the general case outlined in Section 2.2, the only boundary condition that needs to be derived with asymptotic homogenization is the one concerning temperature, and additionally, as it will be clarified later, it is not necessary to solve *ad hoc* auxiliary problems to retrieve the thermal slip coefficient in the case of a smooth delimiting solid boundary.
Sufficiently close to the wall, the velocity is small enough to have no heat transfer by convection, but only by conduction. Therefore, the temperature in both the solid and the fluid will be governed by the Laplace's equation. Two non-dimensional temperatures θ and ϕ associated, respectively, with the fluid and the solid, and the dimensionless microscopic coordinates are defined as follows:

$$\theta = \frac{\hat{T}}{\hat{\mathcal{T}}_C}, \quad \phi = \frac{\hat{\mathcal{T}}}{\hat{\mathcal{T}}_C}, \quad x_i = \frac{\hat{x}_i}{e} \tag{2.17}$$

So the problem equations and the boundary conditions can be rewritten:

$$\begin{cases} \dfrac{\partial^2 \theta}{\partial {x_j}^2} = 0, & \text{in fluid domain } (\beta), \\ \dfrac{\partial^2 \phi}{\partial {x_j}^2} = 0 & \text{in solid domain } (\sigma), \\ \phi = 1 & \text{at } \mathcal{I}_C, \\ \theta = \phi, \ \ \frac{\partial \theta}{\partial n} = \kappa \frac{\partial \phi}{\partial n} & \text{at } \mathcal{I}_{\sigma\beta}, \end{cases} \tag{2.18}$$

plus a condition to match the fluid temperature of the microscopic and macroscopic problem, $\lim_{x_2 \to \infty} \theta = \lim_{X_2 \to 0} \Theta$ (where $X_i = \hat{x}_i / H$ corresponds to the dimensionless macroscopic coordinate).
The microscopic dependent variables, θ and ϕ, are asymptotically expanded in terms of $\epsilon = e/H$, for the microscopic problem to be later reconstructed at the different orders:

$$\begin{aligned} \theta &= \theta^{(0)} + \epsilon \theta^{(1)} + ... \\ \phi &= \phi^{(0)} + \epsilon \phi^{(1)} + ... \end{aligned} \tag{2.19}$$

Generally, the variables in the expansions are dependent on both x_i and X_i. These expressions are then substituted into the system 2.18 and the problem at the leading order ($\mathcal{O}(\epsilon^0)$) reads:

$$\begin{cases} \dfrac{\partial^2 \theta^{(0)}}{\partial {x_j}^2} = 0, & \text{in fluid domain } (\beta), \\ \dfrac{\partial^2 \phi^{(0)}}{\partial xj^2} = 0 & \text{in solid domain } (\sigma), \\ \phi^{(0)} = 1 & \text{at } \mathcal{I}_C, \\ \theta^{(0)} = \phi^{(0)}, \ \frac{\partial \theta^{(0)}}{\partial n} = \kappa \frac{\partial \phi^{(0)}}{\partial n} & \text{at } \mathcal{I}_{\sigma\beta}, \\ \dfrac{\partial \theta^{(0)}}{\partial x_2} = 0 & \text{at } x_2 \to \infty \end{cases} \tag{2.20}$$

A trivial solution exists for the problem: $\theta^{(0)} = 1$ constant over the fluid phase and $\phi^{(0)} = 1$ constant over the solid phase.
The problem at order ϵ is written as follows:

$$\begin{cases} \dfrac{\partial^2 \theta^{(1)}}{\partial {x_j}^2} = 0, & \text{in fluid domain } (\beta), \\ \dfrac{\partial^2 \phi^{(1)}}{\partial xj^2} = 0 & \text{in solid domain } (\sigma), \\ \phi^{(1)} = 0 & \text{at } \mathcal{I}_C, \\ \theta^{(1)} = \phi^{(1)}, \ \frac{\partial \theta^{(1)}}{\partial n} = \kappa \frac{\partial \phi^{(1)}}{\partial n} & \text{at } \mathcal{I}_{\sigma\beta}, \\ \dfrac{\partial \theta^{(1)}}{\partial x_2} = \eta(X_i), \quad \eta(X_i) = \dfrac{\partial \Theta^{(1)}}{\partial X_2} & \text{at } x_2 \to \infty, X_2 \to 0 \end{cases} \tag{2.21}$$

Thanks to linearity, a generic solution can be assumed in the form:

$$\begin{aligned} \theta^{(1)} &= \tilde{\theta}(x_i) \ \eta(X_i) \\ \phi^{(1)} &= \tilde{\phi}(x_i) \ \eta(X_i) \end{aligned} \tag{2.22}$$

The new purely microscopic fields, $\tilde{\theta}$ and $\tilde{\phi}$ solves the following Laplace's equations:

$$\begin{aligned} \frac{d^2 \tilde{\theta}}{dx^2} &= 0 \\ \frac{d^2 \tilde{\phi}}{dx^2} &= 0 \end{aligned} \tag{2.23}$$

where x is intended as the direction normal to the solid wall surface. The total derivative is employed since heat conduction occurs mainly in the x direction, while it is negligible in

comparison in the other directions. The following boundary conditions are applied, where x_0 corresponds to the fluid-solid interface, $x = 0$ to the outer solid surface and $x = 1$ to the matching interface between macroscopic and microscopic problems:

$$\begin{aligned}
&\tilde{\phi}\,(x=0) = 0 \\
&\tilde{\phi}\,(x=x_0) = \tilde{\theta}\,(x=x_0) \\
&\left.\frac{d\tilde{\theta}}{dx}\right|_{x=x_0} = \kappa \left.\frac{d\tilde{\phi}}{dx}\right|_{x=x_0} \\
&\left.\frac{d\tilde{\theta}}{dx}\right|_{x=1} = 1
\end{aligned}$$

The solution of the governing equations is:

$$\begin{aligned}
\tilde{\theta} &= C_1 x + C_2 \\
\tilde{\phi} &= C_3 x + C_4
\end{aligned} \tag{2.24}$$

and applying the boundary conditions, it gives:

$$\begin{aligned}
\tilde{\theta} &= x + \left(\frac{1}{\kappa} - 1\right) x_0 \\
\tilde{\phi} &= \frac{1}{\kappa} x
\end{aligned} \tag{2.25}$$

Since $\kappa = k_s/k_f$ and the solution is sought at the interface between solid and fluid region, it is sufficient to calculate one of the two equations at $x = x_0$, yielding:

$$\tilde{\theta}|_{x_0} = \frac{k_f}{k_s} x_0 \tag{2.26}$$

Substituting Eq. 2.26 in the generic solution for first order problem $\mathcal{O}(\epsilon^1)$ for θ, one obtains:

$$\theta^{(1)} = \frac{k_f}{k_s} x_0 \;\; \eta(X_i) \tag{2.27}$$

Ahmed et al.[4] have found that taking the temperature to $\mathcal{O}(\epsilon^2)$ under steady conditions leads to microscopic parameters which vanish at the matching interface, and thus, do not contribute to the effective temperature boundary condition.
So inserting Eq. 2.27 in the power series of the non-dimensional fluid temperature:

$$\theta = \theta^{(0)} + \epsilon\theta^{(1)} + \mathcal{O}(\epsilon^3) \approx 1 + \epsilon\eta\tilde{\theta} = 1 + \epsilon\eta \frac{k_f}{k_s} x_0 \tag{2.28}$$

Eq. 2.28 is used to define the homogenized boundary condition at the fluid-solid interface, which in dimensional form is:

$$\hat{T} = \hat{\mathcal{T}}_C + e\,\frac{k_f}{k_s}\,\frac{d\hat{T}}{d\hat{x}}\bigg|_{\hat{x_0}} \tag{2.29}$$

where $\hat{\mathcal{T}}_C$ is the temperature at the base of the solid layer, e the thickness of the solid layer and k_f/k_s the thermal conductivity ratio. So in the case of a plate with a smooth surface, the dimensional thermal slip coefficient $\Lambda_\theta = e\frac{k_f}{k_s}$ has an analytical solution. This condition will be implemented in *OpenFOAM* and tested through a comparison with complete CHT simulations in the next chapters.

3 | Simulations set-up

The scope of this work is to assess the capability of the homogenized boundary condition derived in reproducing the results obtained through a full-featured conjugate heat transfer simulation. In the pursuit of basic validation, the analytical solution for the smooth surface configuration, as delineated in Section 2.2.1, is initially tested on simple geometries, before its application to the more complex case of the human nasal airways.
For each case examined in this thesis, CHT simulations are conducted, followed by a comparative analysis between the results obtained from these simulations and from the homogenized-based approach. Notably, in the case of nasal flow analysis, an additional simulation is carried out, imposing a constant temperature at the interface. Throughout this thesis, the entirety of CFD simulations is steady-state Reynolds-averaged Navier-Stokes (RANS).
The software employed for mesh generation and simulation execution is *OpenFOAM*, version 10. Within this chapter, a detailed exposition is provided regarding the setup of the simulations, including the creation of geometric models and the procedure of mesh generation.

3.1. Model

The first necessary step to perform a numerical simulation is to create the model which will be later discretized, in order to generate the computational grid.

3.1.1. Simple channels

The simple channels are created using the CAD software *OnShape*. The geometries selected are a straight channel, a convergent-divergent duct and an elbow pipe with a convergent at the outlet, all characterized by a smooth surface interface between the solid and fluid region. These specific geometries are chosen for their resemblance to shapes commonly found within the human nasal anatomy.
The geometrical parameters are presented in Figure 3.1 and Table 3.1. Furthermore, to comprehensively explore the capabilities and limitations of the homogenized boundary

condition, four distinct solid layer thicknesses are examined for each case: 1 mm, 5 mm, 10 mm and 15 mm.

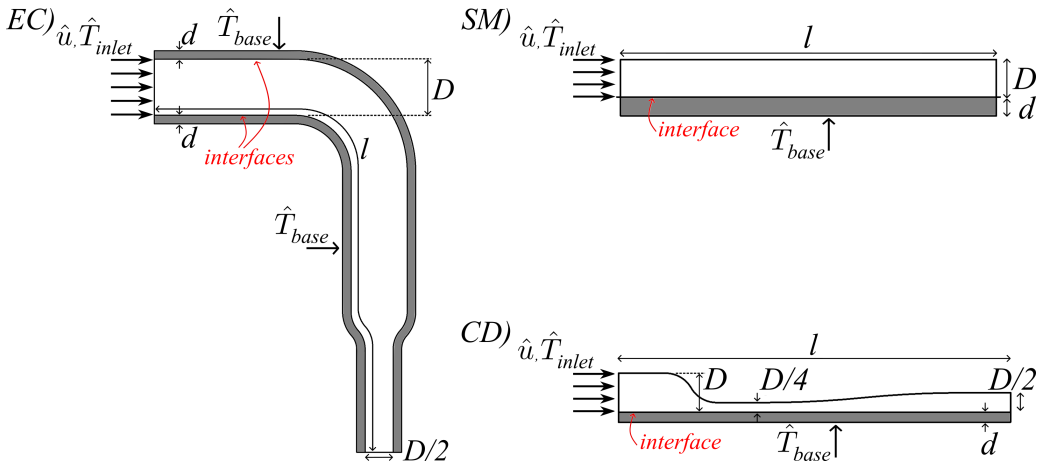

Figure 3.1: The simple smooth channels are characterized by: D channel diameter, d solid layer thickness, l channel length. The geometries are characterized by acronyms chosen as follows: *EC)* is Elbow-Convergent, *SM)* is SMooth straight channel and *CD)* is Convergent-Divergent.

Config.	D $[mm]$	l $[mm]$
EC	10	105
SM	10	100
CD	20	200

Table 3.1: Dimensions of the simple channels.

3.1.2. Human nose

The reconstruction of a three-dimensional model of a patient's airways begins with the acquisition of X-ray images of the area of interest through a CT scan. These images are then utilized to reconstruct the 3D model using the software *3D Slicer*. This procedure has been extensively covered in previous thesis works [9, 14, 18] and by Quadrio et al. [19], where the reliability of CFD simulation results using a model acquired with this method was demonstrated. Additionally, a threshold for radiodensity levels to be employed in CT scans has been identified to ensure that the characteristics of the global flow are not affected by it. In this study, the employed 3D model, shown in Figure 3.2, does not include the frontal and paranasal sinuses and is further altered using the software

Autodesk Meshmixer. The modifications involve smoothing the geometry, to reduce the number of details in order to achieve a meshable geometry, and incorporating a spherical air volume surrounding the external nose. This latter addition serves to relocate the inlet area of the computational domain away from the nostrils. For the upper airways model intended for CHT simulation, the internal airways are encircled by an outer solid layer, representing the respiratory mucous. For this tissue, a constant thickness of 0.5 mm has been chosen, as done by Wu et al. [24], who use a similar model but apply it to the lower airways, and by [16]. It is important to emphasize that the air passage ducts are characterized by a diameter smaller than 1 mm in some areas of the nasal cavity, making the assumption of length scale separation somewhat delicate in those regions. A constant temperature value of 37 $^{\circ}C$ will be imposed on the outer wall of the entire solid layer, based on the assumption that beneath this layer, the network of blood vessels is dense enough to maintain the surrounding tissue at body temperature [1]. The mucous layer is modeled as a layer of water and the same approximation is also made in [13, 16, 24]. This simplification can be considered acceptable, since mucus consists of 90-95% water [8], and the underlying pseudo-stratified epithelium, that enables its production, is also rich in water. This outer solid layer is omitted in simulations employing a constant temperature and a homogenized boundary condition.

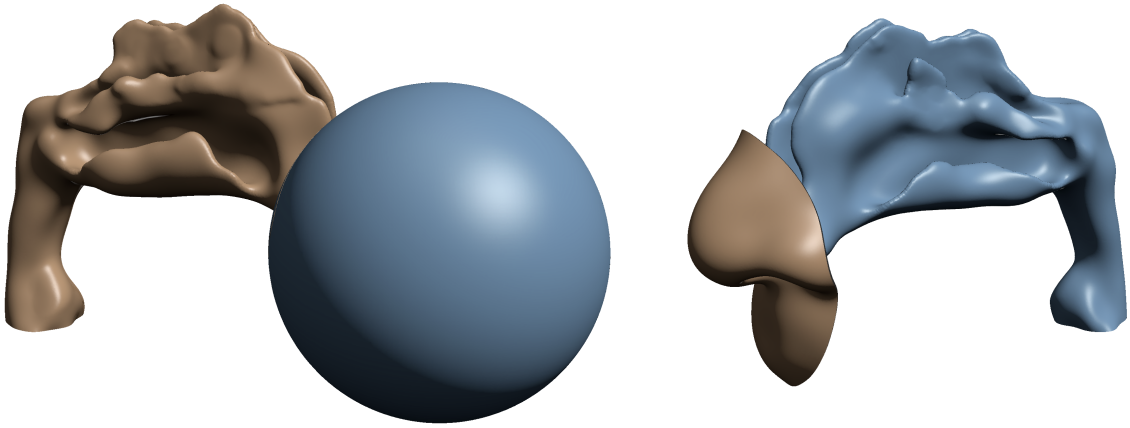

(a) (b)

Figure 3.2: 3D nose model including the external air volume around the nose tip (Figure 3.2a) and the interface between the mucous layer and air region (Figure 3.2b).

3.2. Grid generation

The volume mesh generation is performed using multiple *OpenFOAM* utilities. A background mesh containing the geometry is created using `blockMesh`. The utility `snappyHex-`

`Mesh` is used for modifying the background mesh to adapt it to the geometry and to refine it around the features of interest, according to the quality parameters defined in the dictionary (for instance a maximum skewness of 4 and maximum non-othogonality of 55°). In the simple channels cases, the domain is bi-dimensional, so `extrudeMesh` is used to create a 2D mesh. Lastly, `splitMeshRegions` is employed for separating the fluid and solid regions, when CHT simulations are performed. In Figure 3.3, the result of the mesh after the split operation is shown for a coronal section of the nose and in Table 3.2, the number of cells obtained for the various geometries is reported. For a meaningful comparison, it is crucial to maintain consistency in the mesh utilized across the compared cases. Therefore, the homogenization-based simulations are carried out copying the mesh of the fluid region used in the corresponding CHT simulations.

	Cells number		
Config.	Fluid	Solid	Total
SM (1 mm)	29850	5586	35436
CD (1 mm)	24017	3319	27336
EC (1 mm)	25784	4958	30742
NOSE	9363381	6072961	15436342

Table 3.2: Number of cells of the meshes. For the simple channels, only the number of cells of the solid region for 1 mm thickness is presented.

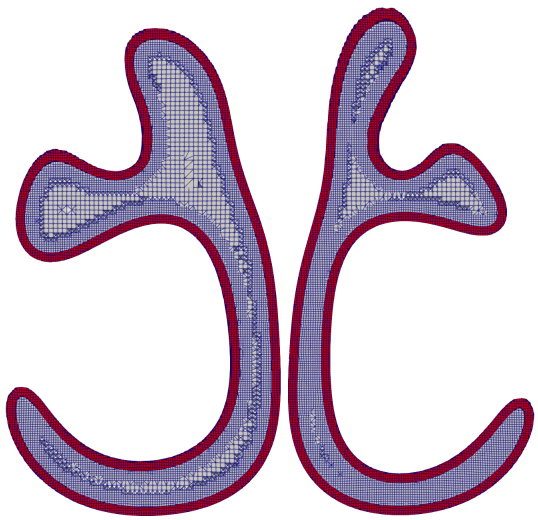

Figure 3.3: Mesh detail on a coronal section of the nose. The red represents the solid layer and the grey the fluid region.

3.3. Solver settings

The airflow inside the fluid region is governed by Navier-Stokes equations (conservation of mass, momentum, and energy) along with the ideal gas thermodynamic model. According to this model, enthalpy can be expressed as a function of temperature, $dh = c_p dT$, where density ρ, thermal conductivity k_f, kinematic viscosity ν, and specific heat c_p are considered constants, as aforementioned in Section 2.1. Turbulence is modeled using the Reynolds-averaged Navier-Stokes (RANS) approach. The RANS equations for the incompressible and steady-state case are reported, where $\overline{(\cdot)}$ represents the mean component and $(\cdot)'$ the fluctuating one of the problem variables:

$$\nabla \cdot \overline{\mathbf{u}} = 0 \tag{3.1}$$

$$(\overline{\mathbf{u}} \cdot \nabla)\,\overline{\mathbf{u}} + \nabla \cdot \left(\overline{\mathbf{u}'\mathbf{u}'}\right) = -\frac{1}{\rho}\nabla \overline{p} + \nu \nabla^2 \overline{\mathbf{u}} \tag{3.2}$$

$$(\overline{\mathbf{u}} \cdot \nabla)\,\overline{T} + \nabla \cdot \left(\overline{\mathbf{u}'T'}\right) = \nabla \cdot \left(\frac{k_f}{\rho c_p}\nabla \overline{T}\right) \tag{3.3}$$

Additional terms are present with respect to the Navier-Stokes equations: $\overline{u'u'}$ in the momentum equation and $\overline{u'T'}$ in the energy equation, representing respectively the mean of the velocity fluctuations and the mean of the velocity and temperature fluctuations. These terms require the introduction of a closure model. Here, the two equations RNG $k-\epsilon$ model, where the turbulent viscosity is based on the Boussinesq assumption, is chosen. The RNG $k-\epsilon$ turbulence model is formulated through the application of "renormalization group" (RNG) methods to the Navier-Stokes equations. This mathematical technique results in a model with different constants and additional terms in the transport equations for turbulence kinetic energy (k) and dissipation rate (ϵ), compared to the standard $k-\epsilon$ model. The RNG approach provides an analytical expression for the turbulent Prandtl number, whereas the traditional $k-\epsilon$ model relies on empirically chosen constant values. Additionally, the RNG model offers a differential formula for effective viscosity, derived analytically, enabling it to handle low-Reynolds-number and near-wall flows more effectively than the standard $k-\epsilon$ model [25]. This choice has also been driven by the convergence difficulty encountered when using the $k-\omega$ SST model in simulations involving conjugate heat transfer. The $\overline{u'T'}$ term is modeled analogously to Boussinesq's assumption: it is assumed to be proportional to the gradient of the mean temperature field via a coefficient α_t, representing turbulent thermal diffusivity, $\overline{u'T'} = \alpha_t \nabla \overline{T}$. The coefficient α_t is further expressed as a function of turbulent kinematic viscosity according

to the relation $\alpha_t = \nu_t/Pr_t$, where the term in the denominator is the turbulent Prandtl number. As stated previously, in the case of a fully-featured CHT simulations it is also necessary to investigate the solid region, where only heat transfer by conduction is observed. In addition, it is required to couple fluid and solid equations by the condition of temperature and heat flux continuity applied at the interface separating the two zones, already presented in Section 2.1.
The thermophysical properties selected for the fluid and solid regions are specified in Table 3.3. In all simulations conducted, air is chosen as the fluid, while for the solid layer a distinction is made: in the case of simple channels, it is characterized by wood properties, whereas in the case of the nose, it represents the mucous layer, which has the same properties as water.

Air		
ρ	1.293	$[kg/m^3]$
k_f	0.026	$[W/(m \cdot K)]$
c_p	1004.9	$[J/(kg \cdot K)]$

Wood		
ρ	800	$[kg/m^3]$
k_s	0.1	$[W/(m \cdot K)]$
c_v	1760	$[J/(kg \cdot K)]$

Mucous		
ρ	993.36	$[kg/m^3]$
k_s	0.598	$[W/(m \cdot K)]$
c_v	4181	$[J/(kg \cdot K)]$

Table 3.3: Fluid and solid properties for the simple channels cases (air, wood) and for the human nose (air, mucous).

The solver employed for simulations involving conjugate heat transfer is `chtMultiRegionFoam`, a computational tool designed to manage both steady-state and transient fluid dynamics, as well as solid heat conduction, while incorporating conjugate heat transfer phenomena between the different regions. The coupling between fluid and solid domains follows this strategy: initially, fluid equations are solved, using the solid temperature from the previous iteration to establish boundary conditions for fluid temperature. Subsequently, solid equations are solved, utilizing the fluid temperature from the prior iteration to prescribe boundary conditions for solid temperature. This iterative process persists until convergence is achieved. Whereas, for simulations incorporating the homogenized boundary condition, as well as those with constant wall temperature, the `rhoSimpleFoam` solver is employed for solution computation. This solver is a steady-state solver for compressible, in order to include the energy equation solution, turbulent flow, utilizing the SIMPLE (Semi-Implicit Method for Pressure Linked Equations) algorithm.
Regarding the numerical schemes employed for solving the discretized equations within the fluid region, `cellLimited Gauss linear 1` is used for gradients and laplacians, while `bounded Gauss linear-Upwind` is utilized for divergence terms. Within the solid region, `Gauss linear` and `Gauss linear limited 1` are respectively deployed for gradients and laplacians.

3.4. Boundary conditions

The computational solvers employed require the specification of initial and boundary conditions. Within the fluid domain, conditions are necessary for pressure, velocity, temperature and turbulent quantities, in cases where laminar flow is not assumed. Employing the $RNG\ k-\epsilon$ turbulence model entails imposing conditions for turbulent kinetic energy k, turbulent dissipation rate ϵ, turbulent kinematic viscosity ν_t and turbulent thermal diffusivity α_t. For complete CHT simulations, boundary conditions must be enforced also for the solid domain, wherein heat transfer is solely by conduction, thus, temperature is the only quantity under consideration.
Regarding velocity, in the context of simple channel flows, a velocity aligned with the x-axis ($\hat{u}$) is prescribed at the domain inlet, as detailed in Table 3.4, in order to achieve the desired Reynolds number. In simulations pertaining to nasal flow, it is chosen to force the flow by assigning a constant velocity in the throat with a value which causes a flow rate of a resting condition, corresponding to $16\,l/min$ [21].

Config.	$\hat{u}\ [m/s]$	Re
SM	0.15	100
CD_{lam}	0.075	100
CD_{turb}	3	4000
EC	0.15	100

Table 3.4: Inlet velocities and Reynolds numbers ($Re = \dfrac{\hat{u}D}{\nu}$) for the simple channels cases. For the convergent-divergent channel is reported the Re at the throat section.

Regarding temperature specification, it is necessary to impose a temperature value at the fluid domain inlet. For the smooth simple channels, $\hat{T}_{inlet}$ is set to 280 K, whereas for the nasal case, various external environment temperatures are examined to investigate the efficacy of the homogenization-based simulation to replicate the results obtained with a complete CHT one in diverse real-life scenarios. Initially, the temperature is set to 280 K, subsequently varied to 260 K, 300 K and 320 K.
In the fully-featured CHT cases, the condition `compressible::turbulentTemperatureCoupledBaffleMixed` must be enforced at the interface, ensuring temperature and thermal flux continuity between the fluid and solid regions. Furthermore, a constant temperature at the outer layer of the solid region is imposed, consistently set to 310 K across all CHT simulations. In contrast, in simulations employing the boundary condition derived in Section 2.2.1, it is necessary first and foremost to implement it within *OpenFOAM*.

To do so, two files are written in this work: `homTempFvPatchScalarField.H`, for defining the variables, and `homTempFvPatchScalarField.C`, for compiling the boundary condition (further implementation details are provided in Appendix A). The condition is named `homTemp` and in order to be used in simulations, the boundary condition will be written as depicted in Listing 3.1 and applied at the fluid boundary corresponding to the interface between solid and fluid regions.

```
fluid_to_solid
    {
      type                        homTemp; //boundary condition name
      kF                            0.026; //fluid thermal conductivity
      kS                            0.598; //solid thermal conductivity
      solidThickness               0.0005; //solid layer thickness
      baseTemperature       uniform 310; //outer solid layer temperature
      value                 uniform 310;
    }
```

Listing 3.1: Interface boundary condition with the homogenized boundary condition.

4 | Results

In this chapter, the results for both simple channel cases and the human nose case are presented. The former are utilized for validating the boundary condition obtained through homogenization for a solid layer characterized by a smooth surface interface, whereas the nose case represents the focal point of this thesis. The aim is to ascertain whether the model derived in Chapter 2 effectively reproduces the outcomes obtained from a complete CHT simulation, without encountering the complications associated with it, such as an increased mesh complexity and computational cost, while maintaining greater result accuracy compared to a constant wall temperature condition.

4.1. Simple channels

In pursuit of basic validation of the homogenized boundary condition in the limiting case of channels with a smooth surface interface, three pipes in which the delimiting solid boundary has no protrusions are considered. The analytical solution for this configuration, obtained in Section 2.2.1, is tested in a laminar smooth channel, a laminar and turbulent convergent-divergent duct and an elbow pipe with a convergent at the outlet. For each geometry, four different solid layer thicknesses are tested: $1\,mm$, $5\,mm$, $10\,mm$ and $15\,mm$, to assess the limits of the homogenized boundary condition.
In Figure 4.1, the results are depicted. The graphs illustrate the temperature distribution along the solid-fluid interface for the different geometries and for each solid thickness, considering both the conjugate heat transfer and the homogenization-based scenarios. It is evident that the results exhibit a high degree of agreement, especially for smaller solid thicknesses, and this is a promising result for the applicability to the human nose case, where the solid layer is particularly thin. For the smooth channel the maximum absolute error E, sufficiently far from the inlet section, goes from $0.025\,K$ for $1\,mm$ (the percentage error relative to the temperature difference in the domain, $310\,K - 280\,K = 30\,K$, is equal to 0.08%) to $0.08\,K$ for $15\,mm$ (0.27%). For the laminar convergent-divergent channel, after the flow is fully developed, E ranges from $0.011\,K$ (0.037%) to $0.06\,K$ (0.2%). While for the turbulent case it goes from $0.073\,K$ (0.24%) to $0.6\,K$ (2%). In

the elbow channel, the greatest discrepancy between the results obtained with CHT and the homogenized boundary condition occurs. Indeed, the absolute error reaches 4.3 K (14.3%) for a solid thickness of 15 mm, 3 K (10%) for 10 mm, 1.5 K (5%) for 5 mm, and 0.1 K (0.3%) for 1 mm. This behavior is expected from the theory of homogenization, which predicts more accurate results for small values of the scale separation ratio, which in practice means thinner solid thicknesses. Additionally, it can be noted that besides the thickness of the solid layer, the geometry of the problem also influences the accuracy of the boundary condition. Specifically, the case with a higher error is the EC, where the interface is not a flat plate but presents curved surfaces, since the boundary condition is derived for a flat plate geometry.

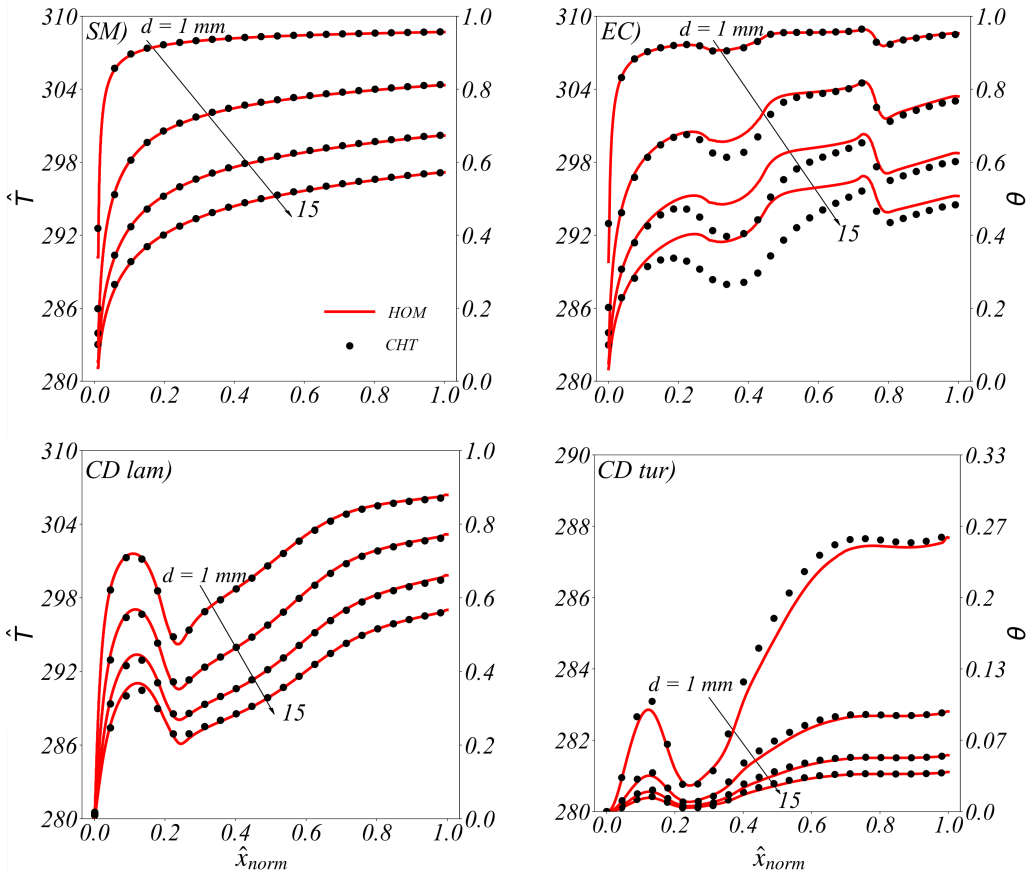

Figure 4.1: The results for the smooth channels are represented; four different thicknesses d are applied to the solid layer (1, 5, 10 and 15 mm). On the abscissa the normalized x-coordinate ($\hat{x}_{norm}$) is plotted, on the left and right ordinate are plotted respectively the dimensional ($\hat{T}$) and non-dimensional (θ) temperatures. The sampling is performed at the solid-fluid interface. For the case EC) the sampling is performed at the lower interface. SM) are the results for the laminar smooth channel, EC) for the laminar elbow convergent, CD lam) for the laminar and CD tur) for the turbulent convergent divergent.

4.2. Human nose

This section presents a comparative analysis between results obtained with complete CHT simulations and those generated through the homogenization-based approach, with a specific focus on assessing the latter's accuracy in modeling nasal flow dynamics. It is important to underscore the clinical significance of accurately identifying the coldest regions within the nasal cavity surface tissue. Areas characterized by lower temperatures are of particular clinical interest, as they are associated with an elevated risk of bleeding. Notably, this phenomenon remains unaddressed when employing a constant wall temperature boundary condition. The comparison of results is carried out at various ambient temperature, aiming to analyse the potential impact of temperature difference within the domain on the fidelity of the model developed in this study.

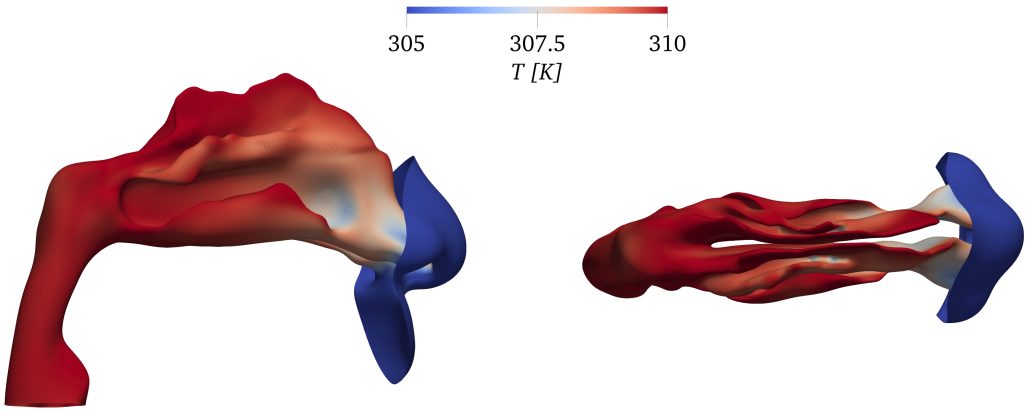

Figure 4.2: Temperature distribution in the case of homogenized solution (HOM) over the solid-fluid interface ($T_{inlet} = 280\ K = 7\ °C$).

Firstly, an environmental temperature of $7\ °C$ is selected, since it deviates sufficiently from the body temperature, yet still remains around a value that occurs quite commonly. In Figure 4.2, the temperature values along the interface, separating solid and fluid regions, are shown for the simulation where the homogenized boundary condition at the interface is applied (HOM). The greatest differences from body temperature are observed on the surface of the nose directly in contact with the external environment and in the vestibular area, thus in the areas furthest from the naso-pharynx, where the approximation of a constant temperature of $37\ °C$ can be considered acceptable. As also noted by [16], there is a temperature drop to around $33\ °C$ in correspondence to the beginning of the middle and inferior turbinates. These areas are characterized by a concave surface protruding into the nasal airflow, causing the air to strike them almost perpendicularly, maximizing heat exchange. To analyze the internal temperature field, it is useful to observe the

sagittal sections of the left and right nostrils (Figure 4.3). It can be noticed how a large part of the heating of the air occurs in the region of the turbinates, to then reach a temperature of 35.6 $°C$ in the naso-pharynx, in accordance with what was observed in [17, 20].

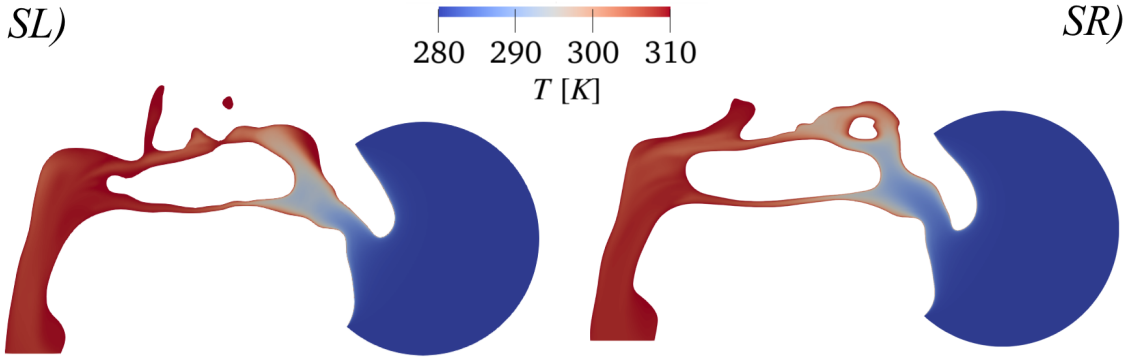

Figure 4.3: Temperature field in the case of homogenized solution (HOM) on two sagittal sections across left (SL) and right (SR) nostrils ($T_{inlet} = 280\ K = 7\ °C$).

The results obtained from the HOM simulation are compared with those obtained from a full CHT simulation to assess their accuracy. As can be seen from Figure 4.4, the homogenized boundary condition works well in reproducing the effect of the mucous layer without the need to simulate it. In fact, within the internal domain, temperature differences are between $0\ °C$ and $\pm 0.1\ °C$, with the maximum temperature discrepancy being around $0.3\ °C$ in coronal section *3*. This corresponds to a difference of 1% relative to the temperature jump present within the domain, which is of $30\ °C$ ($310\ K - 280\ K = 37\ °C - 7\ °C$). In general the biggest differences occur where the surface curvature is very high or in the narrower sections.

Using the homogenization-based approach resulted in approximately a 30% reduction in computational time compared to the full CHT case (14 hours versus 20 hours) and a 40% decrease in RAM usage (15 GB versus 26 GB), given the significantly lower number of mesh cells without the solid layer. However, the main advantage lies in the creation of the geometric model. Prior to achieving a correct mesh for the CHT case, a lengthy trial-and-error process was required, beginning with simplifying the geometry to prevent self-intersections caused by adding the solid layer. Subsequently, iterative modifications to both the model and *OpenFOAM* mesh generation settings were necessary to obtain a mesh with acceptable quality and proper cell allocation in the solid and fluid regions. All these challenges can be overcome with the use of the homogenized boundary condition, as it does not require adding the solid layer, thereby also allowing for the use of a more detailed airway model.

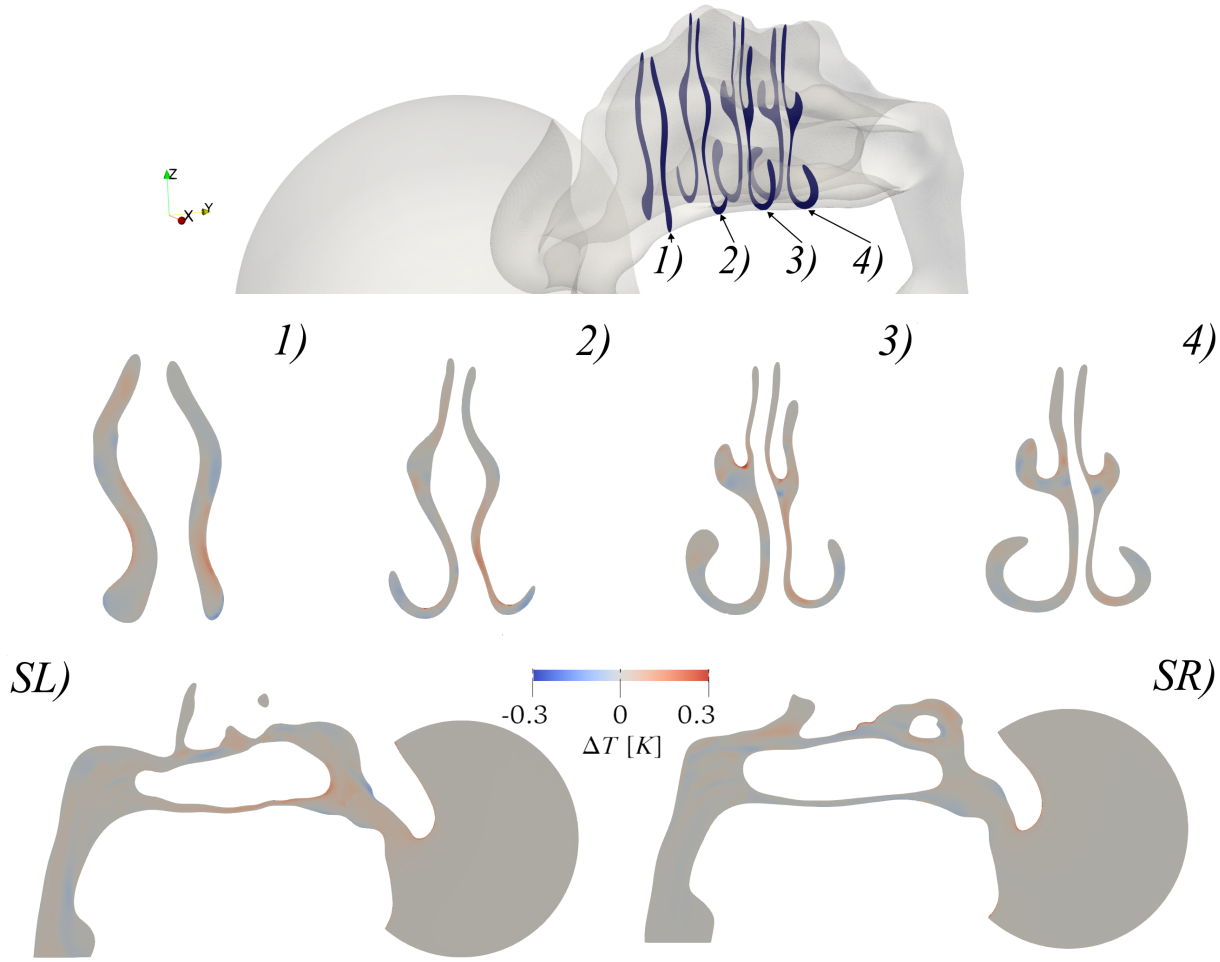

Figure 4.4: Temperature difference between the case of homogenized solution and the full featured CHT ($T_{HOM} - T_{CHT}$), on four coronal sections, shown in the picture above, and on two sagittal slices across left (SL) and right (SR) nostrils ($T_{inlet} = 280\,K = 37\,°C$). The ΔT range corresponds to $\pm 1\%$ of the temperature jump in the domain ($30\,K$).

For the case of the nose, a simulation is also conducted by imposing a boundary condition of constant temperature of $37\,°C$ ($Tfix$) at the interface between mucous and air, to demonstrate how it fails to reproduce the results of a full CHT simulation compared to when the homogenized boundary condition (HOM) is used. Despite the complexity of mesh generation and the computational cost of $Tfix$ and HOM being comparable and lower with respect to the CHT case, it can be appreciated that the performance of the latter is better in terms of reproducing the results obtained with a full conjugate heat transfer simulation. While in the case of constant temperature at the interface, significant differences compared to the CHT case can be observed, reaching up to $2\,°C$, in a much broader region. As illustrated in Figure 4.5, these differences are mainly observed in the

central region, starting from the beginning of the turbinates, especially at the narrower sections, and in the vestibule.

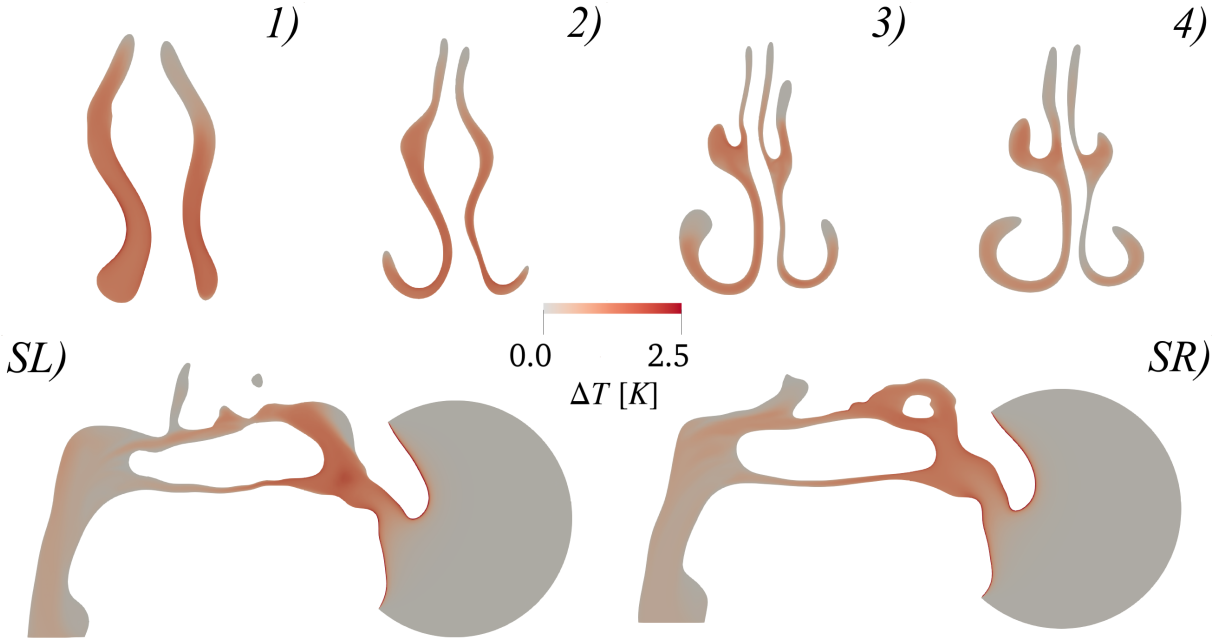

Figure 4.5: Temperature difference between the case of fixed boundary temperature and the full featured CHT ($T_{Tfix} - T_{CHT}$), on four coronal sections and on two sagittal slices across left (SL) and right (SR) nostrils ($T_{inlet} = 280\ K = 37\ °C$).

Subsequently, an external temperature of $-13\ °C$ is tested to observe the temperature difference trend between the HOM and CHT simulations as the temperature jump within the domain increases; indeed, it is equal to $50\ °C$ ($310\ K - 260\ K = 37\ °C - (-13\ °C)$) in this case. In Figure 4.6, the error distribution is represented. The absolute error is greater compared to the case where the external temperature is $7\ °C$; in this scenario, the maximum error reaches $0.5\ °C$. However, expressing the error as a percentage of the temperature jump, it can be noticed that the trend is almost identical to Figure 4.4. So also in this case, the maximum discrepancy is 1% and is reached in the same areas.
The trend is also confirmed in the scenario of a reduced temperature jump in the domain. As a matter of fact, as the ambient temperature is set to $27\ °C$ (Figure 4.7), the maximum error recorded is around $0.1\ °C$, which corresponds to 1% of the temperature jump in the domain, which is equal to $10\ °C$.

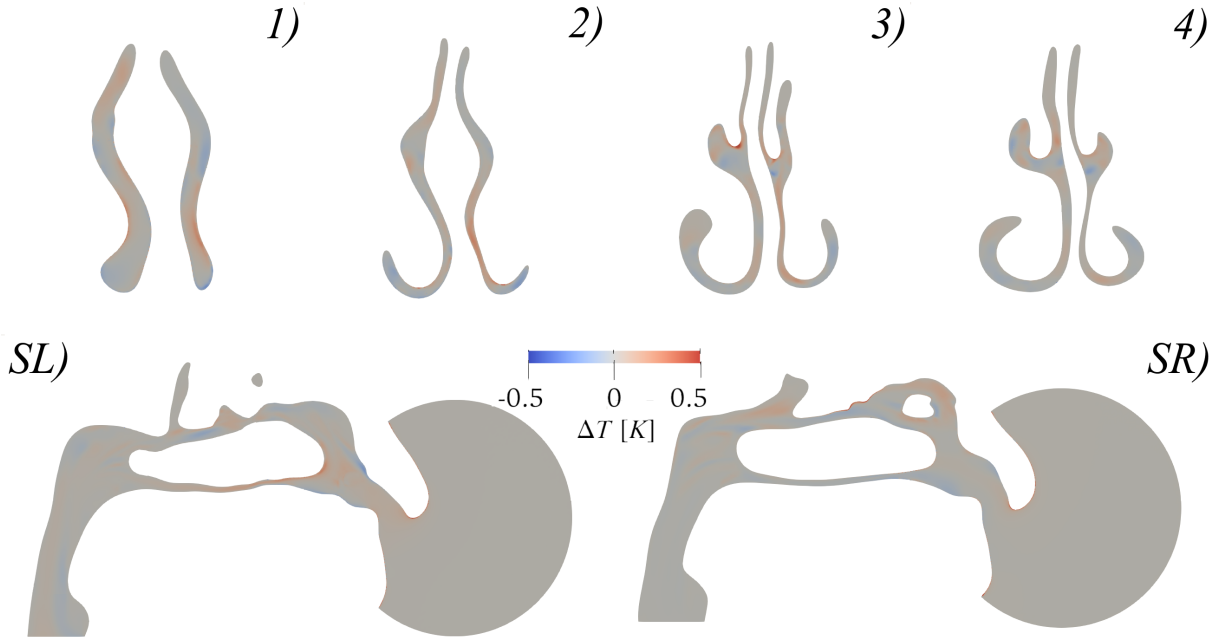

Figure 4.6: Temperature difference between the case of homogenized solution and the full featured CHT ($T_{HOM} - T_{CHT}$) for $T_{inlet} = 260\ K = -13\ °C$. The ΔT range corresponds to $\pm 1\%$ of the temperature jump in the domain ($50\ K$).

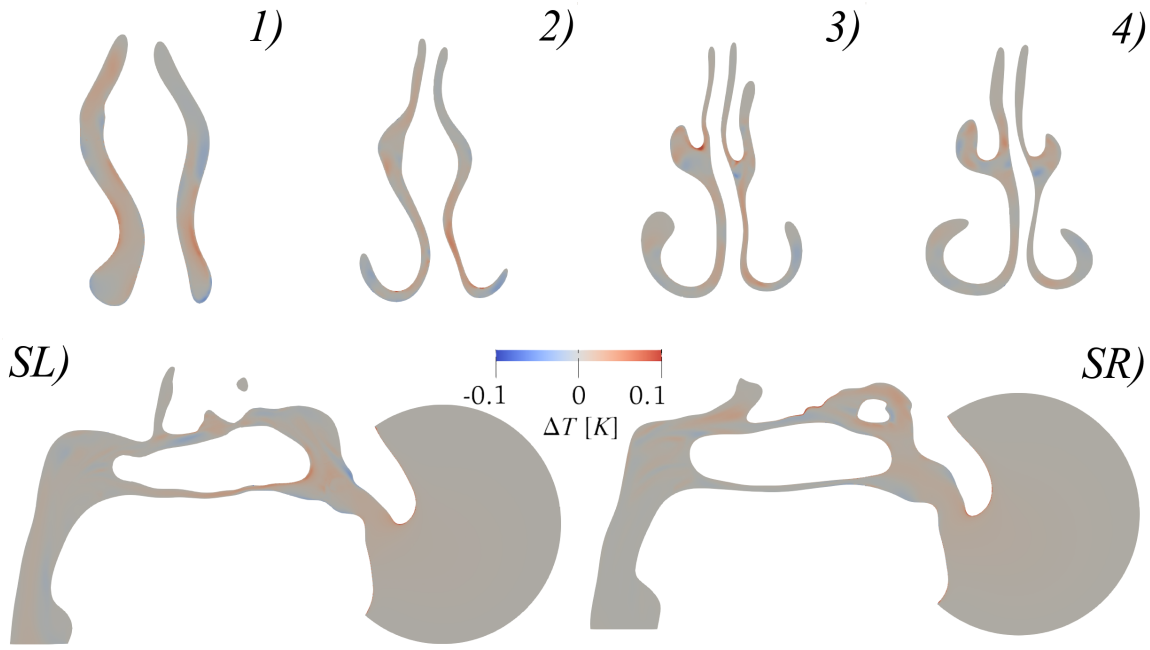

Figure 4.7: Temperature difference between the case of homogenized solution and the full featured CHT ($T_{HOM} - T_{CHT}$) for $T_{inlet} = 300\ K = 27\ °C$. The ΔT range corresponds to $\pm 1\%$ of the temperature jump in the domain ($10\ K$).

The behaviour of the homogenized boundary condition is also investigated when the external temperature is higher than the body temperature. For this reason, it is decided to test its behavior at an ambient temperature of 47 $°C$. This choice is made to have the same temperature difference in the domain as in the case at 27 $°C$, with opposite sign, and is still a temperature that can occur in particularly hot climates. As shown in Figure 4.8, in the left nostril, the error trend is almost identical to that of the 27 $°C$ case but with the opposite sign. This suggests that the heating and cooling of the air operated by the nose are symmetric. However, in the right nostril, especially in the vestibule area and at the beginning of the turbinates, the difference is slightly greater.

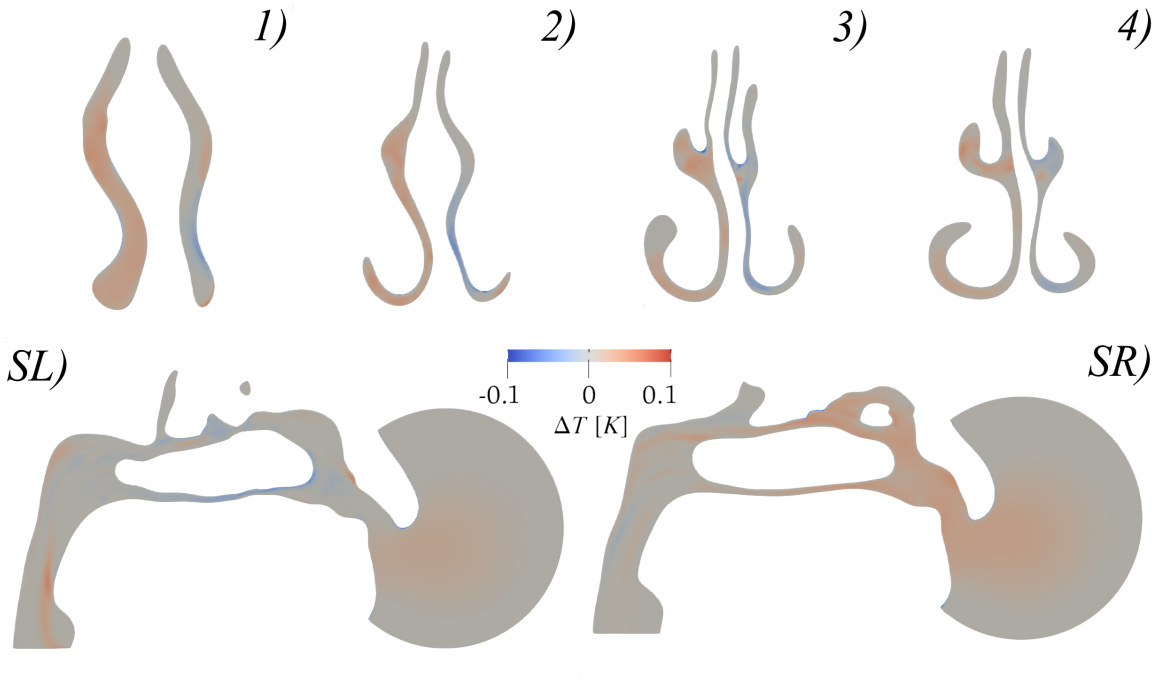

Figure 4.8: Temperature difference between the case of homogenized solution and the full featured CHT ($T_{HOM} - T_{CHT}$) for $T_{inlet} = 320\ K = 47\ °C$. The ΔT range corresponds to $\pm 1\%$ of the temperature jump in the domain ($10\ K$).

It is decided to investigate further the nose cooling mechanism to see if the difference in the error trend is related to this aspect. The nose cooling mechanism is analyzed comparing the results obtained for an environmental temperature of 47 $°C$ with the ones obtained at an external temperature of 27 $°C$. In Figure 4.9, the difference between the calculated temperature and a reference temperature of 37 $°C$ is shown for the two different external temperatures, both for the complete CHT case and for the case where the homogenized boundary condition is employed. Observing the images, it can be seen how qualitatively the nose cooling and heating process seems symmetric, both for CHT and

homogenization-based simulations; indeed, there is the same temperature difference, in absolute value, in the vestibule and turbinate regions, where in both cases most of the heating/cooling of the inspired air occurs. In all cases, the temperature reached in the naso-pharynx is close to the body temperature, ensuring that the air reaching the lungs is always optimal.

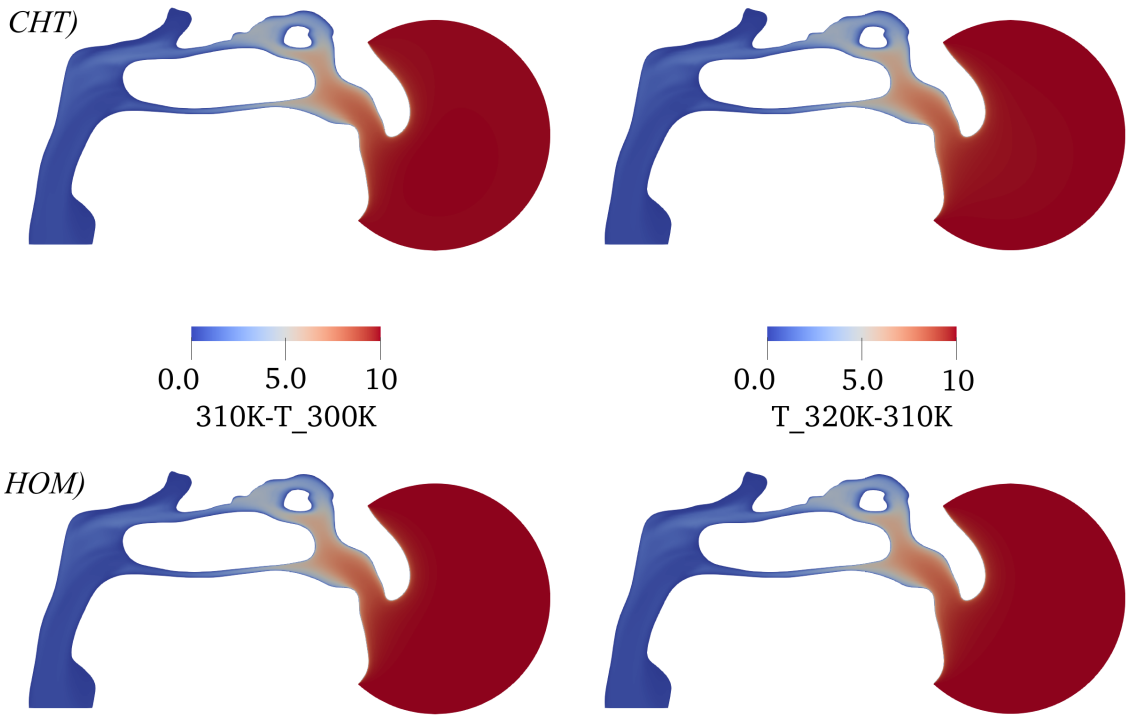

Figure 4.9: Temperature difference for the temperature calculated for $T_{inlet} = 300\ K = 27\ ^{\circ}C$ and $T_{inlet} = 320\ K = 47\ ^{\circ}C$ with respect to a reference temperature of $310\ K = 37\ ^{\circ}C$.

Subtracting the fields obtained in Figure 4.9, it is possible to understand in a more quantitative manner whether the heating and cooling processes inside the nose are indeed symmetric. As seen in Figure 4.10, the maximum difference recorded is a tenth of a degree, and generally, a higher difference is obtained in the right nostril with CHT simulations. This also explains the different error trends obtained for an external temperature of 47 $^{\circ}C$, as illustrated in Figure 4.8. This slightly different temperature trend in the case of nose cooling could be explained by the greater difficulty of convergence observed in CHT simulations with an input temperature higher than body temperature. Indeed, with the same number of iterations, the residuals are slightly higher and the temperature difference is more pronounced especially in the external air domain, which is not very

realistic during inspiration. However, a more detailed analysis regarding the nose cooling mechanism is required in any case.

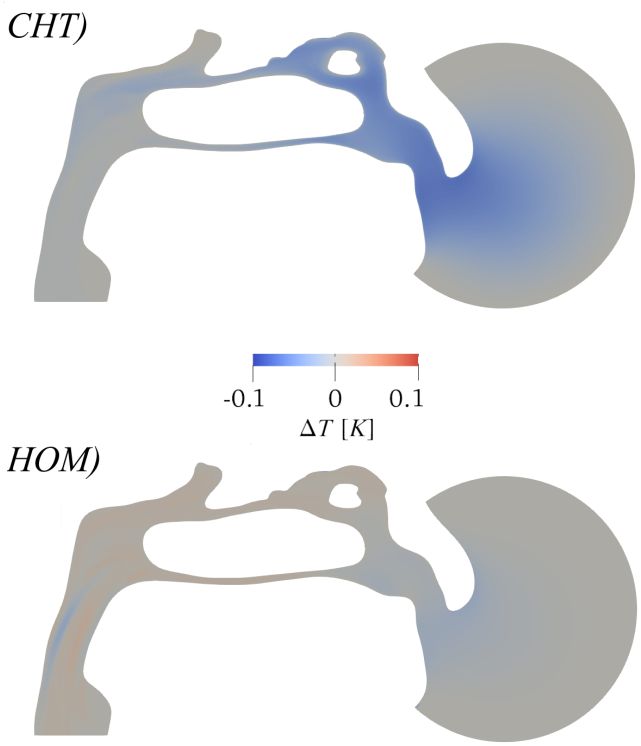

Figure 4.10: Subtractions of the fields obtained in Figure 4.9, $(T_{320K} - 310K) - (310K - T_{300K})$.

5 | Conclusions

In this thesis, an analytical equivalent boundary condition, capable of predicting temperature distribution analogously to a full featured CHT, for thin and smooth solid layers, is derived through homogenization theory. This equivalent boundary condition for the temperature field is imposed on the interface between the air and the mucous layer regions to mimic the presence of the layer without actually simulating it. The homogenized boundary condition is firstly implemented in *OpenFOAM* and then validated with simple channel geometries. The results, obtained with homogenization-based and fully-featured CHT simulations, exhibit a strong agreement, particularly for thinner solid layers.
Afterward, the derived boundary condition is applied to the more complex nasal airflow. The computed error, defined as the difference between the temperature calculated with simulations employing the homogenized boundary condition and with complete CHT simulations, is found to increase, as the temperature jump between the external environment and the human body increases. However, the relative percentage error with respect to the temperature jump remains almost constant, reaching a maximum of 1% in only some sections of the nose that are particularly thin and highly curved, without ever exceeding a temperature difference of a few tenths of a degree with respect of a complete CHT. Therefore, it can be stated that the accuracy of the results obtained with a simulation using the homogenized boundary condition is greater compared to those obtained by imposing a constant temperature condition of 37 $^{\circ}C$ at the interface, where the differences with respect to a CHT simulation are equal to a few degrees.
Furthermore, the use of the homogenization-based approach allows for cost and computational time savings, comparable to those of using a constant temperature condition, compared to the full CHT case. This is because in the former case, it is not necessary to simulate the mucous layer and thus the set of additional equations and the related coupling at the interface. However, the primary advantage lies in creating the geometric model. Before achieving a suitable mesh for the CHT case, it is necessary to oversimplify the geometry to prevent self-intersections caused by adding the solid layer. Then, iterative adjustments are needed to achieve a mesh with acceptable quality and proper cell allocation in the solid and fluid regions. All these challenges can be avoided by using

the homogenized boundary condition, as it eliminates the need for adding the solid layer, allowing for the use of a more detailed airway model, that would result in more accurate outcomes.
Nonetheless, despite the satisfactory results achieved, it must be highlighted that the model is developed only in the case of a solid layer with constant thickness; furthermore, it presents some limitations in presence of high curvature of the solid-fluid interface and in the narrower sections of the nasal cavity, where the assumption of length scale separation becomes somewhat delicate. In addition, a more extensive investigation of the air-cooling process carried out by the nose may be necessary.

Bibliography

[1] MacArthur F. J. D., McGarry G. W. The arterial supply of the nasal cavity. *European Archives of Otorhinolaryngology*, 274:809–815, 2017.

[2] Ahmed E.N. Natural-convection heat transfer from regularly ribbed vertical surfaces: Homogenization-based simulations towards a correlation for the Nusselt number. *Numerical Heat Transfer, Part A: Applications*, 83(9):991–1013, 2023.

[3] Ahmed E.N., Bottaro A. Laminar flow in a channel bounded by porous/rough walls: Revisiting Beavers-Joseph-Saffman. *European Journal of Mechanics / B Fluids*, 103:269–283, 2024.

[4] Ahmed E.N., Bottaro A., Tanda G. A homogenization approach for buoyancy-induced flows over micro-textured vertical surfaces. *Journal of Fluid Mechanics*, 941:A53, 2022.

[5] Ahmed E.N., Bottaro A., Tanda G. Conjugate natural convection along regularly ribbed vertical surfaces: A homogenization-based study. *Numerical Heat Transfer, Part A: Applications*, 2023.

[6] Ahmed E.N., Tanda G. An experimental and numerical study of laminar natural convection along vertical rib-roughened surfaces. *International Journal of Heat and Mass Transfer*, 223:125227, 2024.

[7] Babuška I. Homogenization and its application. Mathematical and computational problems. *Hubbard, B. (Ed.), Numerical Solution of Partial Differential Equations–III*, pages 89–116, 1976.

[8] Bansil R., Turner B. S. The biology of mucus: composition, synthesis and organization. *Advanced Drug Delivery Reviews*, 124:3–15, 2018.

[9] Biondi E. Simulazione LES del flusso nelle cavità nasali. Master's thesis, Politecnico di Milano, 2013-2014.

[10] Bottaro A. Flow over natural or engineered surfaces: an adjoint homogenization perspective. *Journal of Fluid Mechanics*, 877, P1, 2019.

[11] Dinis P., Haider H. Septoplasty: Long-term evaluation of results. *American Journal of Otolaryngology*, 23:85–89, 2002.

[12] Garcia G. J. M., Bailie N., Martins D. A., Kimbell J. S. Atrophic rhinitis: a CFD study of air conditioning in the nasal cavity. *Journal of Applied Physiology*, 103:1082–1092, 2007.

[13] Kim D., Chung S., Na Y. Numerical study on the air conditioning characteristics of the human nasal cavity. *Computers in Biology and Medicine*, 86:18–30, 2017.

[14] Lamberti G., Manara F. Simulazione RANS e LES della fluidodinamica delle cavità nasali. Master's thesis, Politecnico di Milano, 2013-2014.

[15] Lindemann J., Keck T., Wiesmiller K., Sander B., Brambs H.J., Rettinger G., Pless D. A numerical simulation of intranasal air temperature during inspiration. *Laryngoscope*, 114:1037–1041, 2004.

[16] Mangani F. Effetto della temperatura nella fluidodinamica nasale. Master's thesis, Politecnico di Milano, 2019-2020.

[17] Naftali S., Rosenfeld M., Wolf M., Elad D. The Air-Conditioning Capacity of the Human Nose. *Annals of Biomedical Engineering*, 33:545–553, 2005.

[18] Pesci C. OpenNOSE: an open-source procedure for the simulation of nasal aerodynamics. Master's thesis, Politecnico di Milano, 2012-2013.

[19] Quadrio M., Pipolo C., Corti S., Messina F., Pesci C., Saibene A. M., Zampini S., Felisati G. Effects of ct resolution and radiodensity threshold on the cfd evaluation of nasal airflow. *Medical & Biological Engineering & Computing*, 54:411–419, 2016.

[20] Saksono P.H., Nithiarasu P., Sazonov I. Numerical prediction of heat transfer patterns in a subject-specific human upper airway. *Journal of heat transfer*, 134/031022, 2012.

[21] Segalerba E., Dini Ciacci G., Quadrio M., Pralits J. O. On the comparison between pre- and post-surgery nasal anatomies via computational fluid dynamics. *Biomechanics and Modeling in Mechanobiology*, 2023.

[22] Stone H.A., Stroock A.D., Ajdari A. Engineering flows in small devices: Microfluidics towards a lab-on-a-chip. *Annual Reviews of Fluid Mechanics*, 36:381–411, 2004.

[23] Vicenzotti G. Influenza della temperatura nelle vie aeree superiori. Master's thesis, Politecnico di Milano, 2017-2018.

[24] Wu D., Tawhai M. H., Hoffman E. A., Lin C. A numerical study of heat and water vapor transfer in MDCT-based human airway models. *Annals of Biomedical Engineering*, 40:2117–2131, 2014.

[25] Yakhot V., Orszag S. Renormalization Group Analysis of Turbulence: 1. Basic Theory. *Journal of Scientific Computing*, 1:3–51, 1986.

A | Appendix A

This appendix reports the implementation in the OpenFOAM source code of the homogenized boundary condition. To do so, it is necessary to write the file `homTempFvPatchScalarField.H` (Listing A.1), which defines the variables, and the file `homTempFvPatchScalarField.C` (Listing A.2), to compile the boundary condition.

```
#ifndef homTempFvPatchScalarField_H
#define homTempFvPatchScalarField_H
#include "fixedValueFvPatchFields.H"

// * * * * * * * * * * * * * * * * * * * * * * * * * * * * * * * * * * * * * * * * * * * * * * * * * * * * * * * * //

namespace Foam
{

/*---------------------------------------------------------------------------*\
               Class homTempFvPatchScalarField Declaration
\*---------------------------------------------------------------------------*/

class homTempFvPatchScalarField
:
    public fixedValueFvPatchScalarField
{
protected:

    // Protected Data

        const scalar kS_; //- Solid thermal conductivity
        const scalar kF_;  //- Fluid thermal conductivity
        const scalar solidThickness_; //- Solid thickness

        Field<scalar> baseTemperature_; //- Base temperature field

        Field<scalar> oldT;  //- Old temperature value

```

```
30          //- Cell temperature initialization
31      //Field<scalar> Tcell;
32  public:
33
34      //- Runtime type information
35      TypeName("homTemp");
36
37
38      // Constructors
39          //- Construct from patch and internal field
40          homTempFvPatchScalarField
41          (
42              const fvPatch&,
43              const DimensionedField<scalar, volMesh>&
44          );
45
46          //- Construct from patch, internal field and dictionary
47          homTempFvPatchScalarField
48          (
49              const fvPatch&,
50              const DimensionedField<scalar, volMesh>&,
51              const dictionary&
52          );
53
54          //- Construct by mapping given homTempFvPatchScalarField
55          //  onto a new patch
56          homTempFvPatchScalarField
57          (
58              const homTempFvPatchScalarField&,
59              const fvPatch&,
60              const DimensionedField<scalar, volMesh>&,
61              const fvPatchFieldMapper&
62          );
63
64          //- Disallow copy without setting internal field reference
65          homTempFvPatchScalarField
66          (
67              const homTempFvPatchScalarField&
68          ) = delete;
69
70          //- Copy constructor setting internal field reference
71          homTempFvPatchScalarField
72          (
73              const homTempFvPatchScalarField&,
```

```
            const DimensionedField<scalar, volMesh>&
        );

        //- Construct and return a clone setting internal field
    reference
        virtual tmp<fvPatchScalarField> clone
        (
            const DimensionedField<scalar, volMesh>& iF
        ) const
        {
            return tmp<fvPatchScalarField>
            (
                new homTempFvPatchScalarField(*this, iF)
            );
        }


    // Member Functions

        // Evaluation functions
            //- Update the coefficients associated with the patch field
            virtual void updateCoeffs();

        //- Write
        virtual void write(Ostream&) const;
};


} // End namespace Foam

#endif
```

Listing A.1: homTempFvPatchScalarField.H.

```
#include "homTempFvPatchScalarField.H"
#include "addToRunTimeSelectionTable.H"
#include "volFields.H"
#include "surfaceFields.H"
#include "pressureInletOutletVelocityFvPatchVectorField.H"


// * * * * * * * * * * * * * * Constructors  * * * * * * * * * * * * * * //

Foam::homTempFvPatchScalarField::homTempFvPatchScalarField
(
```

```
    const fvPatch& p,
    const DimensionedField<scalar, volMesh>& iF
)
:
    fixedValueFvPatchScalarField(p, iF),
    kS_(0.0),
  kF_(0.0),
    solidThickness_(0.0),
    baseTemperature_(p.size(), 0.0)
{}


Foam::homTempFvPatchScalarField::homTempFvPatchScalarField
(
    const fvPatch& p,
    const DimensionedField<scalar, volMesh>& iF,
    const dictionary& dict
)
:
    fixedValueFvPatchScalarField(p, iF, dict),
    kS_(readScalar(dict.lookup("kS"))),
    kF_(readScalar(dict.lookup("kF"))),
    solidThickness_(readScalar(dict.lookup("solidThickness"))),
    baseTemperature_("baseTemperature", dict, p.size())
{}


Foam::homTempFvPatchScalarField::homTempFvPatchScalarField
(
    const homTempFvPatchScalarField& ptf,
    const fvPatch& p,
    const DimensionedField<scalar, volMesh>& iF,
    const fvPatchFieldMapper& mapper
)
:
    fixedValueFvPatchScalarField(ptf, p, iF, mapper),
    kS_(ptf.kS_),
    kF_(ptf.kF_),
    solidThickness_(ptf.solidThickness_),
    baseTemperature_(ptf.baseTemperature_)
{}


Foam::homTempFvPatchScalarField::homTempFvPatchScalarField
```

```
(
    const homTempFvPatchScalarField& tppsf,
    const DimensionedField<scalar, volMesh>& iF
)
:
    fixedValueFvPatchScalarField(tppsf, iF),
    kS_(tppsf.kS_),
    kF_(tppsf.kF_),
    solidThickness_(tppsf.solidThickness_),
    baseTemperature_(tppsf.baseTemperature_)
{}


// * * * * * * * * * * * * *  Member Functions  * * * * * * * * * * * * * //

void Foam::homTempFvPatchScalarField::updateCoeffs()
{


  // store in "Tp" the field of scalar temperature on the patch
    const scalarField& Tp(patch().lookupPatchField<volScalarField,
   scalar>("T"));

  // store in "Tc" the field of scalar temperature in the computational
   domain
    const scalarField& Tc(patch().lookupPatchField<volScalarField,
   scalar>("T").internalField());
  //Info << "Size of Tc: " << Tc.size() << endl;

  // initialize cell's temperature variable
  scalarField Tcell(Tp.size(), Zero);

  // distance from the face center to the cell center on patch's cells
  const scalarField& deltaInv(patch().deltaCoeffs());

  // separately calculate the homogenization coefficient "lambda_theta"

  const scalarField Coeff(kF_/kS_*solidThickness_*deltaInv);

  // store in "cells" the labels of the cells adjacent to the face
  const labelList cells(patch().faceCells());

  // initialize the counter
  label cellN(0);
```

```
96    forAll(cells, patchCell) {
97      cellN = cells[patchCell];
98      Tcell[patchCell] = Tc[cellN];
99    }
100
101   // face temperature
102   const scalarField faceTemp(( baseTemperature_ + Tcell * Coeff) / ( 1 +
        Coeff));
103
104   // value assigned to the patch
105   operator==
106   (
107     faceTemp
108   );
109
110     fixedValueFvPatchScalarField::updateCoeffs();
111 }
112
113
114 void Foam::homTempFvPatchScalarField::write(Ostream& os) const
115 {
116     fixedValueFvPatchScalarField::write(os);
117
118     writeEntry(os, "kS", kS_);
119     writeEntry(os, "kF", kF_);
120     writeEntry(os, "solidThickness", solidThickness_);
121     writeEntry(os, "baseTemperature", baseTemperature_);
122     writeEntry(os, "value", *this);
123
124 }
125
126 // * * * * * * * * * * * * * * * * * * * * * * * * * * * * * * * * * * * * //
127
128 namespace Foam
129 {
130     makePatchTypeField
131     (
132         fvPatchScalarField,
133         homTempFvPatchScalarField
134     );
135 }
```

Listing A.2: `homTempFvPatchScalarField.C`.

List of Figures

1.1 Respiratory mucous histology inside the human nose. The upper airways are characterized by a thin layer (respiratory mucous) immersed in an airflow, where heat transfer is involved. 2
1.2 Nasal cavity anatomy. 3

2.1 Sketch of the problem under consideration. The plane interfaces delimited by dashed lines constitute the *virtual boundaries* where effective conditions are to be enforced. 6

3.1 The simple smooth channels are characterized by: D channel diameter, d solid layer thickness, l channel length. The geometries are characterized by acronyms chosen as follows: *EC)* is Elbow-Convergent, *SM)* is SMooth straight channel and *CD)* is Convergent-Divergent. 15
3.3 Mesh detail on a coronal section of the nose. The red represents the solid layer and the grey the fluid region. 17

4.1 The results for the smooth channels are represented; four different thicknesses d are applied to the solid layer (1, 5, 10 and 15 mm). On the abscissa the normalized x-coordinate ($\hat{x}_{norm}$) is plotted, on the left and right ordinate are plotted respectively the dimensional ($\hat{T}$) and non-dimensional (θ) temperatures. The sampling is performed at the solid-fluid interface. For the case EC) the sampling is performed at the lower interface. SM) are the results for the laminar smooth channel, EC) for the laminar elbow convergent, CD lam) for the laminar and CD tur) for the turbulent convergent divergent. 23
4.2 Temperature distribution in the case of homogenized solution (HOM) over the solid-fluid interface ($T_{inlet} = 280\ K = 7\ ^\circ C$). 24
4.3 Temperature field in the case of homogenized solution (HOM) on two sagittal sections across left (SL) and right (SR) nostrils ($T_{inlet} = 280\ K = 7\ ^\circ C$). 25

4.5 Temperature difference between the case of fixed boundary temperature and the full featured CHT ($T_{Tfix} - T_{CHT}$), on four coronal sections and on two sagittal slices across left (SL) and right (SR) nostrils ($T_{inlet} = 280\ K = 37\ ^{\circ}C$). 27
4.6 Temperature difference between the case of homogenized solution and the full featured CHT ($T_{HOM} - T_{CHT}$) for $T_{inlet} = 260\ K = -13\ ^{\circ}C$. The ΔT range corresponds to $\pm 1\%$ of the temperature jump in the domain ($50\ K$). 28
4.7 Temperature difference between the case of homogenized solution and the full featured CHT ($T_{HOM} - T_{CHT}$) for $T_{inlet} = 300\ K = 27\ ^{\circ}C$. The ΔT range corresponds to $\pm 1\%$ of the temperature jump in the domain ($10\ K$). 28
4.8 Temperature difference between the case of homogenized solution and the full featured CHT ($T_{HOM} - T_{CHT}$) for $T_{inlet} = 320\ K = 47\ ^{\circ}C$. The ΔT range corresponds to $\pm 1\%$ of the temperature jump in the domain ($10\ K$). 29

List of Tables

3.1 Dimensions of the simple channels. 15
3.2 Number of cells of the meshes. For the simple channels, only the number of cells of the solid region for 1 mm thickness is presented. 17
3.3 Fluid and solid properties for the simple channels cases (air, wood) and for the human nose (air, mucous). 19
3.4 Inlet velocities and Reynolds numbers ($Re = \frac{\hat{u}D}{\nu}$) for the simple channels cases. For the convergent-divergent channel is reported the Re at the throat section. 20

Listings

3.1 Interface boundary condition with the homogenized boundary condition. . 21
A.1 `homTempFvPatchScalarField.H`. 37
A.2 `homTempFvPatchScalarField.C`. 39

Acknowledgements

This thesis work marks the conclusion of a journey characterized by personal commitment and passion, but I owe part of its success to several individuals who have supported me in many ways, making it possible.

I offer my most heartfelt and sincere gratitude to my family for their encouragement and support during this challenging journey. To my parents, Simona and Paolo, for all the sacrifices they have made to let me pursue my dream and for always believing in me. To my brother Carlo, who is the absolute best flat mate and has been a constant source of amusement and motivation, especially in the last three years.

I would also like to thank my supervisors, Professor Quadrio and Professor Pralits, for giving me the opportunity to participate in this thesis. And a special thanks goes to Eric Segalerba, whose support and encouragement have been of fundamental importance during the toughest moments of this work, never letting me lose heart and without whom I probably wouldn't have been able to complete this research.

Lastly, I wish to express my gratitude to all my friends, from Siena and from Milan, that have contributed in making even the toughest days of these years bearable, as well as creating some memorable moments along the way, with the hope of continuing to share dramas and laughter.